On the accuracy of the measured and modelled surface latent and sensible heat flux in the interior of the Greenland Ice Sheet

Ida Haven[1,2], Hans Christian Steen-Larsen[1,3], Laura J. Dietrich[1,3], Sonja Wahl[1,3,4], Jason E. Box[5], Michiel R. van den Broeke[2], Alun Hubbard[6,7], Stephan T. Kral[1,3], Joachim Reuder[1,3], and Maurice van Tiggelen[2]

[1]Geophysical Institute, University of Bergen, Bergen, Norway
[2]Institute for Marine and Atmospheric research Utrecht, Utrecht University, Utrecht, The Netherlands
[3]Bjerknes Centre for Climate Research, Bergen, Norway
[4]Laboratoire des Sciences du Climat et de l'Environnement, IPSL-CEA-CNRS-UVSQ, Université Paris-Saclay, Gif-sur-Yvette, France
[5]Geological Survey of Denmark and Greenland (GEUS), Copenhagen, Denmark
[6]Geography Research Unit, University of Oulu, Oulu, Finland
[7]Centre for Ice, Cryosphere, Carbon & Climate, Institutt for Geovitenskap, UiT - the Arctic University of Norway, Tromso

Correspondence: Ida Haven (idahaven@kpnmail.nl) and Hans Christian Steen-Larsen (Hans.Christian.Steen-Larsen@uib.no)

Abstract. The latent (LHF) and sensible (SHF) heat fluxes are key components of the surface mass and energy balance in the accumulation area of the Greenland Ice Sheet, making them critical for accurate sea level projections. While Eddy-Covariance (EC) systems provide accurate measurements of the turbulent surface transport of mass and energy in the low and mid-latitudes, frequent stable boundary layer conditions in polar regions introduce uncertainties in the EC method. In addition, as EC mea-
surements are sparse, it is critical to characterise biases in the more common bulk fluxes obtained from automatic weather stations and climate models in polar areas. In this study, we present an intercomparison of three independent EC systems from the 28th of May 2019 until the 31st of July 2019 at the EastGRIP site at $\sim 2700\,\mathrm{m}$ a.s.l on the Greenland Ice Sheet to assess the accuracy of LHF and SHF measurements. A comparison of the fluxes by the three systems demonstrates excellent agreement with an absolute bias of $0.2\,\mathrm{W\,m^{-2}}$ and slopes between 1.01 and 1.16 for the LHF, and an absolute bias of less than $0.5\,\mathrm{W\,m^{-2}}$
and slopes of 1.0 for the SHF. A comparison of the validated EC fluxes against the bulk method highlights the sensitivity to the site-specific roughness length $z_{0,m}$ and the limitation of common parameterisations of the humidity and temperature roughness lengths $z_{0,q}$ and $z_{0,t}$. Using improved values for $z_{0,m}$, $z_{0,q}$ and $z_{0,t}$, recomputed bulk fluxes are compared to fluxes simulated by regional climate models MAR, RACMO2.3p2 and RACMO2.4p1 for the period from 2016 to 2020. We find an overall good agreement between the measured and modelled turbulent flux magnitudes for the summer period; however, all evaluated models simulate stronger near-surface temperature gradients during winter compared to observations from automatic weather stations, leading to consistently larger modelled SHF and LHF values in winter.

1 Introduction

The Greenland Ice Sheet is currently the main single contributor to global ocean mass changes (Otosaka et al., 2023) and, together with the Antarctic Ice Sheet, the biggest source of uncertainty in predicting future sea level rise (Fox-Kemper et al., 2021). Aschwanden et al. (2019) and Plach et al. (2019) show that one of the main uncertainties in accurately simulating past variations and future projections of the volume of the ice sheet is related to inaccuracies of the surface mass balance (SMB). The turbulent latent heat flux (LHF) directly impacts the SMB by adding or removing water through surface evaporation/sublimation and condensation/deposition and linking the mass balance to the surface energy balance (SEB). A thorough understanding of the ice sheet SEB and its impact on SMB is therefore fundamental, particularly across the interior regions of the Greenland Ice Sheet where annual precipitation rates are low and the LHF can act seasonally as a key driver in the SMB (Dietrich et al., 2024). Furthermore, recent research on ice core climate reconstruction (e.g. Dietrich et al., 2023; Wahl et al., 2022) has documented the importance of accurate observations and simulations of LHF for quantifying the impact of post-depositional processes on the water isotope climate signal in the snow. This illustrates the broad need for reliable observations and simulations of the SMB across the Greenland and Antarctic Ice Sheet.

Regional climate models (RCMs) can provide year-round simulations of the surface turbulent heat fluxes. However, it has been documented that they struggle to represent the sensible (SHF) and latent heat flux components of the surface mass balance appropriately (Noël et al., 2018; Dietrich et al., 2024). As a result of quasi-permanent radiative cooling of the interior ice sheet surface, the atmospheric surface layer is usually stably stratified and shallow, and characterized by low temperatures and humidity content and a relatively smooth snow surface. The resulting low magnitude of the turbulent fluxes and the occurrence of steep gradients of temperature, moisture and wind in the atmospheric surface layer, make it an extremely challenging environment for the RCMs. Model evaluations of turbulent heat fluxes in the accumulation zone of the ice sheet are scarce (Ettema et al., 2010), mainly due to the lack of robust and accurate direct observations of the turbulent exchange in the atmospheric surface layer (Miller et al., 2018), resulting in a standstill in the models' skill to represent the turbulent fluxes. Besides their spatial and temporal scarcity, the uncertainty of turbulent flux measurements over the ice sheet themselves poses a challenge to improving the models' representations.

The established standard method for measuring turbulent fluxes is based on the eddy covariance (EC) technique (Swinbank, 1951; Mauder et al., 2021). Wind and temperature fluctuations are typically measured at high temporal resolution ($10 - 50\,\mathrm{Hz}$) using a sonic anemometer, along with humidity variations using an open or closed path water vapour analyser. However, both suffer from limitations as open path analysers experience less attenuation than closed path analysers, but open path analysers are more sensitive to disturbances such as precipitation (Polonik et al., 2019). The SHF and the LHF can be directly calculated as the covariance of vertical velocity fluctuations, and the corresponding temperature and humidity fluctuations, respectively. Yet, the considerable logistic requirements with respect to reliable (over-winter) power supply, supervision and maintenance, allow only rather limited deployments in remote areas under such extreme, polar meteorological conditions. Corresponding EC data sets for the ice sheet are therefore sparse (Van Tiggelen et al., 2021, 2024) and generally limited to summertime deployments.

Year-round observational estimates of SHF and LHF can be obtained by using bulk methodology (e.g. Sun et al., 1999), based on flux-gradient relationships formulated by application of Monin-Obukhov similarity theory (MOST). Mean values of wind speed, temperature and humidity measured by an automatic weather station (AWS), combined with additional information or assumptions on surface temperature and surface humidity, and empirical, stability dependent drag coefficients, based on MOST, allow for an estimation of SHF and LHF even if meteorological variables are only available from one level. The existing limitations in the validity of MOST, in particular for moderately and strongly stable atmospheric conditions (e.g., Grachev et al., 2005; Cullen et al., 2007; Schlögl et al., 2017; Pfister et al., 2019), which are common on top of the Greenland Ice Sheet during winter (Cullen and Steffen, 2001), are expected to increase uncertainty for corresponding SHF and LHF bulk estimates. This is because vertical turbulent mixing becomes limited with increased stability, and non-local phenomena, like gravity waves and inertial oscillations, may occur. The uncertainty of the bulk method under stable conditions is also corroborated by studies that found that the bulk method leads to an underestimated LHF both at the edge of the Greenland Ice Sheet (Box and Steffen, 2001) and on the Antarctic Ice Sheet (Town and Walden, 2009). Additional sources of uncertainty are the dependency of the bulk method on the surface roughness length, which is highly variable across the ice sheet (Van Tiggelen et al., 2021), and indications of flux underestimation by the bulk method in conditions of drifting and blowing snow (Sigmund et al., 2022).

Despite these problems, the bulk method is to date fundamental for the year-round estimation of turbulent heat fluxes, both by meteorological measurements and model simulations. The LHF can in theory also be directly measured by an evaporation pan (Box and Steffen, 2001), however, the method is time-consuming to execute and prone to issues like excessive heating, limited snowfall and blowing snow. A simultaneous direct determination of LHF and SHF can only be provided by the EC technique. Although tested and documented to be accurate under non-polar conditions (Mauder and Zeeman, 2018; Wang et al., 2016; Loescher et al., 2005; Schmidt et al., 2012; Polonik et al., 2019), an intercomparison of multiple independent EC systems at a polar site, in particular focusing on the LHF accuracy, has not been conducted to date.

The aim of this study is to address this knowledge gap, and to determine the accuracy of EC measurements at a high elevation on a polar ice sheet. Using the validated EC measurements, we aim to improve the local bulk flux estimates and evaluate estimated fluxes from RCMs. This goal is achieved by conducting a comparison of the near-surface LHF and SHF measured by three co-located EC systems during the summer of 2019 at the EastGRIP fieldsite and comparing our results with other EC intercomparison studies. The validated EC measurements are then used to provide an observationally-based value for the roughness length at the site. This yields an improved estimate of the turbulent heat fluxes based on the bulk method. The improved year-round record of bulk estimates from 2016 to 2020 is then compared to the output from the high-resolution Regional Atmospheric Climate Model (RACMO) and Modèle Atmosphérique Régional (MAR).

2 Data

2.1 Measurement site

All data used in this study has been collected at the location of the East Greenland Ice Core Project (EastGRIP) field site ($75°37'47''$ N, $35°59'22''$ W). EastGRIP is located in the north-eastern part of the Greenland Ice Sheet (Fig. 1a), in the katabatic wind zone, and approximately 350 km NNE of Summit, the highest point of the ice sheet. The local time is set to UTC-2 and UTC-1 during daylight saving time. In this study, all times are given in UTC and the sign convention is positive for upward fluxes, corresponding to sublimation for the LHF. The observational data comes from three EC systems, installed upwind of the EastGRIP camp, an AWS that is part of the Programme for Monitoring of the Greenland Ice Sheet (PROMICE, station name "EGP", Fausto et al., 2021), and an AWS that is part of GC-Net (station name "EastGRIP", Vandecrux et al., 2023). Both AWSs are located in the vicinity of the EastGRIP camp with sufficient distance to rule out flow disturbance by the campsite (approximately 500 m and 1000 m distance for the GC-Net and PROMICE AWS, respectively). The three EC systems were installed at 2.15 m height in a dedicated clean-snow area, set approximately 6 m apart perpendicular to the dominant wind direction, with the instruments facing into the wind (Fig. 1b and 1c). The clean-snow area is a designated limited-access area oriented away from camp in the direction of the main wind direction to ensure undisturbed snow conditions.

We present observational data from the three EC systems sampled during the period from the 28th of May 2019 until the 31st of July 2019. During this period, the PROMICE AWS recorded a mean air temperature of $-10.2\,°C$, ranging from -25.9 to $1.3\,°C$ and a mean air pressure of 730 hPa. The mean windspeed was $4.5\,\mathrm{m\,s^{-1}}$, with a maximum of $13.7\,\mathrm{m\,s^{-1}}$, an average direction of $254°$, and strong directionality due to the katabatic winds (Fig. 1b). The specific humidity was on average $2.2\,\mathrm{g\,kg^{-1}}$, ranging from $0.5\,\mathrm{g\,kg^{-1}}$ to $5.0\,\mathrm{g\,kg^{-1}}$. A model comparison is done for the 4-year period from 2016-2019, during which both data from the PROMICE AWS and MAR simulation are available. During this period the PROMICE AWS recorded an average temperature of $-27.6\,°C$, ranging from $-63.3\,°C$ to $1.3\,°C$, a mean air pressure of 720 hPa and an average windspeed of $5.3\,\mathrm{m\,s^{-1}}$, with a maximum of $21.3\,\mathrm{m\,s^{-1}}$. The average wind direction during this 4-year period was $242°$, with 74% of the time the wind direction falling within the $200-280°$ sector. All values are based on hourly averaged data.

2.2 Eddy-Covariance systems

The data for the EC comparison comes from three individual EC setups. The first EC system is a combination of a CSAT3 sonic anemometer (Campbell Scientific) and a Krypton Hygrometer 20 (KH20, Fig. 1d, Campbell Scientific). Besides 2019, this EC system was also deployed at EastGRIP during the summers of 2016, 2017 and 2018 (Steen-Larsen et al., a, b, 2022). The second EC system is the IRGASON (Campbell Scientific), hereafter used as reference system, which is a combined sonic anemometer and open-path gas analyser (Fig. 1e). The third system is the combination of a CSAT3 sonic anemometer and a Li-7500 (LI-COR) open-path gas analyser (Fig. 1f).

For all three EC systems, the air temperature measured by the sonic anemometer is used. To measure the humidity fluctuations, the IRGASON and Li-7500 both use infrared absorption, while the KH20 uses absorption of UV radiation, emitted by a krypton lamp. The IRGASON uses radiation at $2.7\,\mu m$ (absorption) and $2.3\,\mu m$ (reference); the Li-7500 uses absorption at
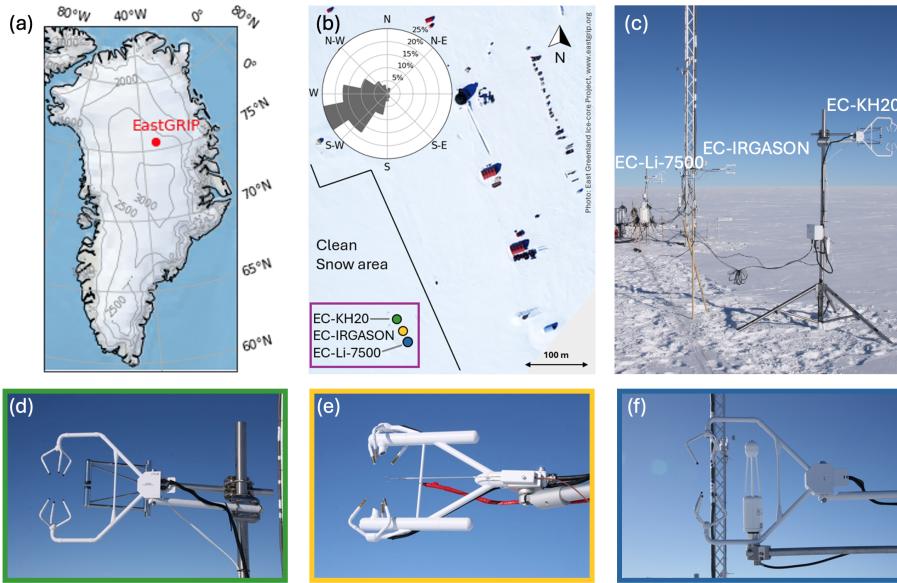
Figure 1. (a) Location of the EastGRIP fieldsite on the Greenland Ice Sheet ($75°37'47''$ N, $35°59'22''$ W), (b) camp overview with the location of the EC-systems in the dedicated clean snow area upwind of the camp along with the windrose during the campaign, (c) overview picture of the three individual EC systems oriented perpendicular to the prevailing wind direction, and detailed views of the individual EC setups (d) CSAT3+KH20 (EC-KH20), (e) IRGASON (EC-IRGASON), (f) CSAT3+Li-7500 (EC-Li-7500). Surface elevation in Fig. 1a is from Morlighem et al. (2017). The footprint of the EC-Irgason is provided in Supplementary Material S1.

2.59 µm and 3.95 µm as a reference; the KH20 uses 123.58 nm along with a minor light at 116.49 nm, both are absorbed by
H$_2$O and O$_2$, and H$_2$O concentration is computed from the combined signal of the two wavelengths. The combined systems of sonic anemometer and hygrometer will be referred to as EC-KH20, EC-IRGASON, and EC-Li-7500. The EC-IRGASON and EC-Li-7500 ran from the 28th of May 2019 until the 31st of July 2019. The EC-KH20 was deployed for three fewer days and ran from the 29th of May until the 29th of July 2019. During this period the EC systems sampled continuously at a frequency of 20 Hz. During the days around the 29th of June and the 1st of July, a combination of snowfall and wind led to measurement issues and consequent gaps in the time series. On the night of the 17th to the 18th of July, possible frosting of the instruments led to a gap in the time series from 2019-07-18 00:00 until 2019-07-18 09:00. The KH20 has a gap in the data from 2019-06-02 14:00 until 2019-06-03 20:00.

Since the EC-KH20 has the longest data availability, the EC-KH20 flux observations from the summers of 2016 to 2019 are used to compare with the model simulations.

2.3 Automatic weather stations

In this study data from two AWSs is used: the PROMICE AWS (Fausto et al., 2021; How et al., 2022) and the GC-Net AWS (Vandecrux et al., 2023; Steffen et al., 2022). The data from the PROMICE AWS is used to compute the LHF and SHF using

the one-level bulk method. The two-level GC-Net data is only used for comparison with the PROMICE data to assess the data quality during winter.

130   The PROMICE AWS was installed on the 1st of May 2016 and has been collecting data uninterruptedly ever since. It measures single-level temperature, wind speed, relative humidity and up- and downwelling shortwave and longwave radiation at approximately $2\,\text{m}$ height above the surface, varying between 1.8 and $2.6\,\text{m}$ due to changes in snow height. Instrument specifications and uncertainties are described in Fausto et al. (2021). For the model comparison, it is assumed that the height is close enough to the $2\,\text{m}$ model output, that it does not need to be corrected (similar to in Dietrich et al., 2024). For specific case

135   studies, the exact measurement height will be provided. The surface temperature is determined using the up- and downwelling longwave radiation and an emissivity of 0.97 (Fausto et al., 2021). The sensitivity of the temperature gradient to the emissivity value is provided in Supplementary Material S2. The surface specific humidity is determined using the surface temperature and assuming saturated conditions relative to ice. Inspection of the relative humidity, temperature and longwave radiation data obtained from the PROMICE station during the winter indicates unrealistic values at temperatures below $-50\,^\circ\text{C}$, i.e. that the

140   relative humidity fully depends on temperature and that occurrences of low temperature (below $-50\,^\circ\text{C}$) take place without simultaneous radiative cooling. Thus, the data with temperatures below $-50\,^\circ\text{C}$ is removed. Further discussion of the data quality in winter is provided in Sect 5.3.

      The GC-Net AWS measures air temperature, relative humidity and wind speed at two vertical levels typically separated by $1.2\,\text{m}$ (instrument specification and uncertainties described in Vandecrux et al., 2023). The distance of the lowest level to the

145   snow surface varied between $0.4\,\text{m}$ and $2.3\,\text{m}$ during the years 2016 to 2019 owing to snow accumulation, compaction and ablation. Instrument heights are provided in the relevant figures.

2.4   RACMO

This study uses two different polar versions of RACMO, a hydrostatic model that combines the atmospheric dynamics of the High Resolution Limited Area Model (HIRLAM, version 5.0.3) with the physics package from the European Centre for

150   Medium-range Weather Forecasts (ECMWF) Integrated Forecast System (IFS) (Noël et al., 2018; Van Dalum et al., 2024). The polar version of RACMO is developed and maintained at the Institute for Marine and Atmospheric Research Utrecht (IMAU) and uses specialised parameterisations to simulate the Arctic and Antarctic climate. Over the Greenland Ice Sheet and surroundings, RACMO is run on a $5.5\,\text{km}$ resolution, with 40 vertical layers. The simulations from both model versions are forced with 3-hourly ERA-5 reanalysis at the lateral boundaries and for both simulations, the output from the gridpoint closest

155   to EastGRIP is analysed.

      The oldest version of RACMO used in this study is RACMO 2.3p2 (Noël et al., 2018, hereafter referred to as RACMO2.3), from which the three-hourly model output is analysed. In RACMO2.3 the ECMWF-IFS physics cycle CY33R.1 is used (Noël et al., 2018). The LHF and SHF are simulated using the bulk method, a constant roughness length for momentum ($z_{0,m}$) of $1 \times 10^{-3}\,\text{m}$ and the Andreas (1987) parameterisation (presented in appendix A) to determine the roughness lengths for moisture

160   ($z_{0,q}$) and heat ($z_{0,t}$) over snow surfaces. In RACMO2.3, the sublimation from blowing snow is included in the surface LHF.

The second version of RACMO is RACMO2.4p1 (Van Dalum et al., 2024, hereafter referred to as RACMO2.4), from which the hourly model output is analysed. One major difference with RACMO2.3 is that in RACMO2.4 the ECMWF-IFS physics package is updated to physics cycle CY47R.1 (Van Dalum et al., 2024) and the blowing snow scheme is improved, as described in Gadde and Van de Berg (2024). The upgraded physics cycle constitutes changes in the precipitation, convection, turbulence, aerosol and surface energy exchange schemes. RACMO 2.4 now uses the IFS radiation physics module ecRad, the new cloud scheme has more prognostic variables, and a multilayer snow module for non-glaciated regions is introduced. A fractional land–ice mask, as well as new and updated climatological data sets (such as aerosol concentrations), are used. The LHF and SHF in RACMO2.4 are simulated in the same way as RACMO2.3. However, sublimation from blowing snow is no longer directly included in the LHF but is stored as a separate variable, and only the surface sublimation is evaluated in this study. The implications of how blowing snow sublimation is handled in the model simulations are discussed in Sect. 4.3.

2.5 MAR

In a similar study by Dietrich et al. (2024), turbulent flux simulations with the RCM MAR (e.g., Fettweis et al., 2017) were evaluated for the EastGRIP site using improved turbulent flux estimates from the PROMICE weather station and the EC-KH20. We show these results alongside the results for the RACMO evaluation in this study. The model data comes from the gridpoint closest to EastGRIP.

In all figures, MAR data (Dietrich, 2023) is presented for the same periods as for RACMO, from between 2016 and 2019. MAR was run on a $30\,\mathrm{km}$ horizontal and 30 vertical layer resolution, which is substantially coarser than in the RACMO simulation. Nonetheless, due to the smooth orography of the accumulation area of the Greenland Ice Sheet, we consider a direct comparison between both simulations for MAR and RACMO valid. As in RACMO, the MAR simulation is forced by the ERA-5 reanalysis product and turbulent fluxes are calculated using a one-layer bulk method with roughness lengths for moisture and heat calculated from the roughness length of momentum following Andreas (1987). However, it should be noted that a constant roughness length of momentum of $1.3 \times 10^{-4}\,\mathrm{m}$ was used for the MAR simulation, much lower than the value of $1 \times 10^{-3}\,\mathrm{m}$ used in the RACMO simulation. Consequently, we would expect lower turbulent flux amplitudes for the MAR output compared to RACMO.

3 Methods

3.1 Eddy-Covariance flux computation

The calculation of fluxes using the EC method requires compliance with EC flux theory and adequate instrumentation. The EC flux technique assumes that transport is turbulence-dominated, with negligible contributions from (sub)meso motion timescales. The method further assumes homogeneity of the terrain, absence of convergence or divergence and stationarity. As the terrain upwind of the EC systems is flat and homogeneous, the EastGRIP field site is well suited for EC measurements. Thus, topography-driven transport regimes are assumed to be negligible and the transport therefore dominated by turbulence. The EC

instrumentation was set up at $2\,\mathrm{m}$ height to ensure measurements were performed in the atmospheric surface layer, which can be shallow in polar, snow-covered conditions.

The EC data is processed using the TK3 software from the University of Bayreuth (Mauder and Foken, 2015). The raw data is filtered using consistency limits of -50 to $50\,\mathrm{m\,s^{-1}}$ for horizontal wind speed (u), -10 to $10\,\mathrm{m\,s^{-1}}$ for vertical wind velocity (w) and -80 to $30\,^{\circ}\mathrm{C}$ for air temperature (T) and spikes are removed using the MAD spike test (Mauder et al., 2013) applying a standard deviation of 3.5. For the EC-KH20 a high number of simultaneous spikes was detected in the measured T and w. These spikes have been removed based on the quality flags provided by the CSAT3. As the focus is on getting accurate fluxes rather than having a complete record, no interpolation is done for the missing values. The raw covariances are calculated using a 10-minute averaging time, cross-correlation and planar fit correction (Wilczak et al., 2001) and are corrected using the Moore (Moore, 1986), WPL (Webb et al., 1980), and the Tanner correction (Tanner et al., 1993) for the EC-KH20. The 10-minute averaging time is chosen based on a modified version (using $30\,\mathrm{min}$ instead of $4\,\mathrm{h}$) of the convergence test by Foken (2006) to ensure the averaging time is suitable for the conditions, i.e. that it is long enough to capture all turbulent variations but does not include (sub)mesoscale effects. The Moore (1986) correction is applied to correct for spectral losses and uses a transfer function based on the Kaimal spectrum (Kaimal et al., 1972), derived from the 1968 Kansas experiment. The use of the Kaimal spectrum for the correction of spectral losses is validated by comparing the shape of w, T, a, $w'T'$ and $w'a'$ (co)spectra to the shape of the Kaimal spectrum (S3 in the supplementary material). After the processing with the TK3 software, remaining outliers in the average flux data are removed by excluding time intervals where u was smaller than $1\,\mathrm{m\,s^{-1}}$ or larger than $8\,\mathrm{m\,s^{-1}}$, or when the absolute value of w was larger than $0.15\,\mathrm{m\,s^{-1}}$ or the wind direction was between $20\,^{\circ}$ and $110\,^{\circ}$ (the direction in which the mounting installation obstructed the flow). Final outliers in the average flux data are removed based on visual inspection. This leaves $84\,\%$ of the 10-min LHF and SHF intervals for the EC-IRGASON, $85\,\%$ of the intervals for the EC-Licor-7500 and $86\,\%$ of the intervals for the EC-KH20. An overview of the time series and the data removed in post-processing is provided in the Supplementary Material (Fig. S4).

3.2 Bulk sensible and latent heat flux computation

To obtain year-round measurements of the LHF and SHF to compare to the regional model output, the turbulent heat fluxes are calculated from the PROMICE AWS observations using the bulk method. We evaluate both the bulk-calculated LHF and SHF provided in the published PROMICE data product (Fausto et al., 2021), as well as re-calculated LHF and SHF using site-specific roughness lengths, against the EC data in summer. Similar to Fausto et al. (2021), we calculate the SHF and LHF using the one-level bulk method, with equations 4 and 5 described in Van As (2011) (note the added minus results from the sign convention used in this study):

$$\mathrm{SHF} = \rho C_p \kappa^2 \frac{u}{\ln\frac{z_u}{z_{0,m}} - \psi_u} \frac{T_\mathrm{s} - T}{\ln\frac{z_t}{z_{0,t}} - \psi_t} \tag{1a}$$

$$\text{LHF} = \rho L_{\text{s}} \kappa^2 \frac{u}{\ln \frac{z_u}{z_{0,m}} - \psi_u} \frac{q_{\text{s}} - q}{\ln \frac{z_q}{z_{0,q}} - \psi_q} \tag{1b}$$

Here ρ is the air density, Cp the specific heat capacity of air at constant pressure, $k = 0.4$ the Von Kármán constant, u the wind speed, T and T_s the temperature measured at $2\,\text{m}$ and at the surface, respectively, L_s the latent heat of sublimation, and q and q_s are the corresponding specific humidities. The surface specific humidity is derived from the surface temperature following the equations in Murphy and Koop (2005), using the equilibrium vapour pressure over ice and assuming saturated conditions. z_u, z_t and z_q are the measurement heights of the wind speed, temperature and humidity and $z_{0,m}$, $z_{0,t}$ and $z_{0,q}$ the roughness lengths of momentum, heat and moisture. ψ_u and ψ_q are the stability correction functions for momentum and moisture, following Holtslag and De Bruin (1988) under stable conditions and the Businger–Dyer expressions, described in Paulson (1970), under unstable conditions. ψ_t and ψ_q are assumed to be the same.

Stable conditions:

$$\psi_u = -\left(0.7\zeta + 0.75\left(\zeta - \frac{5}{0.35}\right)\exp(-0.35\zeta) + 0.75\frac{5}{0.35}\right) \tag{2a}$$

$$\psi_q = \psi_u \tag{2b}$$

Unstable conditions:

$$\psi_u = 2\ln\left(\frac{1+x}{2}\right) + \ln\left(\frac{1+x^2}{2}\right) - 2\tan^{-1}(x) + \frac{\pi}{2} \tag{3a}$$

$$\psi_q = 2\ln\left(\frac{1+x^2}{2}\right) \tag{3b}$$

Where $\zeta = z/L$, L is the Monin-Obukhov length, $x = (1 - \frac{\gamma}{\zeta})^{1/4}$ and $\gamma = 16$ is an empirically derived constant (Paulson, 1970).

The bulk flux formulations require a value for the roughness lengths. For the bulk calculation done by PROMICE a fixed $z_{0,m} = 1 \times 10^{-3}\,\text{m}$ is used for the entire Greenland Ice Sheet together with the parameterisation of Smeets and Van den Broeke (2008a, b) (S&vdB) to determine $z_{0,q}$ and $z_{0,t}$, which are assumed equal. Literature values of roughness lengths above a snow surface cover a wide range of $1 \times 10^{-1}\,\text{m}$ - $1 \times 10^{-5}\,\text{m}$ (Van Tiggelen et al., 2021; Smeets and Van den Broeke, 2008b). To ensure a robust comparison between bulk and EC methods, we use two different methods for determining $z_{0,m}$, $z_{0,t}$ and $z_{0,q}$. The first uses $z_{0,m}$ based on our EC measurements and the Andreas (1987) parameterisation for $z_{0,q}$ and $z_{0,t}$, which are assumed equal. The second method uses $z_{0,m}$, $z_{0,t}$ and $z_{0,q}$ obtained from the EC measurements. The data from the EC-IRGASON is

used, because this system requires no separation correction and provides the most accurate humidity measurements (see Sect. 4.1 and S3 in the supplementary material). It is assumed that the turbulence properties are similar for the other setups, due to the limited separation of $6\,\mathrm{m}$ and the homogeneous terrain. The values for $z_{0,m}$, $z_{0,t}$ and $z_{0,q}$ are estimated using Monin-Obukov similarity and calculated from the measured EC-IRGASON fluxes and the vertical gradients from the PROMICE AWS following Van Tiggelen et al. (2023):

$$z_{0,m} \simeq \frac{z}{\exp\left(\kappa\frac{u(z)}{u_*} + \psi_m\left(\frac{z}{L}\right)\right)}, u_* = \left(\overline{u'w'}^2 + \overline{v'w'}^2\right)^{1/4} \tag{4a}$$

$$z_{0,q} \simeq \frac{z}{\exp\left(\kappa\frac{a(z)-a_s}{a_*} + \psi_m\left(\frac{z}{L}\right)\right)}, a_* = -\overline{w'a'}/u_* \tag{4b}$$

$$z_{0,t} \simeq \frac{z}{\exp\left(\kappa\frac{T(z)-T_s}{T_*} + \psi_h\left(\frac{z}{L}\right)\right)}, T_* = -\overline{w'T'}/u_* \tag{4c}$$

Here z is the height of the EC or PROMICE instruments above the snow surface, which are both $2.15\,\mathrm{m}$ during the measurement campaign in 2019. $u(z)$ is the $2\,\mathrm{m}$ PROMICE wind speed and u_* is the friction velocity, the value of which is based on the EC-IRGASON measurements and provided by TK3. The stability functions are the same as for the bulk calculation. $w'a'$ is the EC-IRGASON covariance of the absolute humidity. Thus, $2\,\mathrm{m}$ and surface saturated specific humidity obtained from the PROMICE AWS are converted to absolute humidity. $w'T'$ is the EC-IRGASON covariance and $T(z)$ and T_s are the $2\,\mathrm{m}$ and surface temperature from the PROMICE AWS. Similar to u_*, the a_* and T_* are turbulent humidity and temperature scales. The 10-minute EC-IRGASON data is averaged to hourly values, to match the PROMICE time resolution. The value for the roughness lengths is then determined by filtering the values for neutral conditions ($-0.02 < z/L < 0.02$) and for $z_{0,m}$ for sufficient wind ($U > 3\,\mathrm{m\,s^{-1}}$) and taking the median. The median is taken due to the large range of magnitude in the results, making the mean unsuitable (see Fig. B1). This gives the following values: $z_{0,m} = 1.3 \times 10^{-4}\,\mathrm{m}$, $z_{0,q} = 5.7 \times 10^{-7}\,\mathrm{m}$ and $z_{0,t} = 2.9 \times 10^{-4}\,\mathrm{m}$. The value for $z_{0,m}$ is similar to the roughness lengths of $1.6 \times 10^{-4}\,\mathrm{m}$ recorded by Van den Broeke et al. (2005b) in the katabatic wind zone in Antarctica.

3.3 Model data processing

RACMO2.3 and RACMO2.4 provide the windspeeds at $10\,\mathrm{m}$ height and in the middle of the lowest layer (also at approximately $10\,\mathrm{m}$ height), respectively. The windspeeds are interpolated to $2\,\mathrm{m}$ height, using the logarithmic wind speed profile and the stability correction functions following the sign convention in Paulson (1970). The surface specific humidity is derived from the surface temperature following the equations in Murphy and Koop (2005), using the equilibrium vapour pressure over ice and assuming saturated conditions.

4 Results

 ### 4.1 Eddy-Covariance flux comparison

The comparison of the LHF measured by the three EC systems over the period 28 May, 2019 to 31 July, 2019 is presented in Fig. 2. It is noteworthy that contrary to the commonly assumed stable atmospheric boundary layer over snow surfaces, in $18\,\%$, $21\,\%$ and $21\,\%$ of the 10-min time intervals measured by the EC-IRGASON, EC-Li-7500 and EC-KH20, respectively, the conditions were unstable (z/L<-0.02). The 8-day time series (Fig. 2a-d) illustrate the diurnal fluctuation of the LHF and the dependence of LHF on specific humidity. Besides following the same general trend and diurnal cycle, Fig. 2 confirms that the three EC systems measure similar sub-hourly LHF variations. Hence, we assume that these observed LHF variations are accurate representations of actual LHF with high signal to noise ratio. Direct comparison of the three instruments (Fig. 2e and 2f) demonstrates high levels of correspondence with correlation coefficient $r = 0.97$ to 0.98, an absolute bias, indicating the mean difference, of $0.2\,\mathrm{W\,m^{-2}}$, and an $RMSE$ between 1.2 and $1.5\,\mathrm{W\,m^{-2}}$. However, the slope of 1.16 in Fig. 2e indicates a substantial difference in the LHF measured by the EC-Li-7500 compared to the EC-IRGASON and EC-KH20 (not shown). This suggests that though the EC-Li-7500 measures the equivalent mean flux as the other two EC systems, it slightly overestimates the amplitude of the daily LHF.

The difference in the LHF measured by the EC-Li-7500 and the two other EC systems can be explained by the humidity measured by the Li-7500 as shown in Fig. 3. A comparison with the PROMICE AWS (Fig. 3), shows an offset in specific humidity between the PROMICE hygrometer and Li-7500. Apart from this offset, a drift over time in the humidity measured by the Li-7500 can clearly be identified (Fig. 3b). This indicates an incorrect and varying sensitivity of the Li-7500, which explains the overestimated LHF measured by the Li-7500 and is likely due to an instrumental problem. In an EC-comparison study by Polonik et al. (2019) in California, in which a.o. an IRGASON and Li-7500A are compared, a similar instrumental problem is reported. In their study the Li-7500A measured $14\,\%$ higher humidity variances than the IRGASON, resulting in a 10 - $28\,\%$ higher LHF than the IRGASON. In their study, the issue was resolved after instrumental repair and recalibration.

A comparison of the SHF measured by the three EC systems (see Fig. 4) shows even higher agreement between the EC systems than the LHF. The SHFs measured by the three EC systems again follow the same diurnal cycle and have similar sub-hourly variations. The direct comparison of the fluxes also indicates a very good agreement between measurement systems ($r = 0.98$, an absolute bias of less than $0.5\,\mathrm{W\,m^{-2}}$, an $RMSE$ between 1.6 and $1.9\,\mathrm{W\,m^{-2}}$, and slopes of 1.0).

 ### 4.2 Bulk-method flux validation

Estimates of the LHF and SHF based on the bulk method in the PROMICE data product are overestimated (Fig. 5), as can be seen by the slopes greater than 1 (Fig. 5a and 5e) and the overestimated amplitude in Fig. 5d and 5h. The overestimated flux magnitudes indicate that the roughness length $z_{0,m} = 1 \times 10^{-3}\,\mathrm{m}$ used in the assessed time period is too high for the EastGRIP location. Using the same $z_{0,m}$ for both the LHF and SHF and assuming $z_{0,q} = z_{0,t}$, leads to a larger overestimation of the LHF than the SHF, with a slope of 2.22 as compared to 1.35 (Fig. 5a and 5e). A separate analysis of only the positive and negative fluxes results in similar slope values (Supplementary Material S5), but similar to Box and Steffen (2001) the
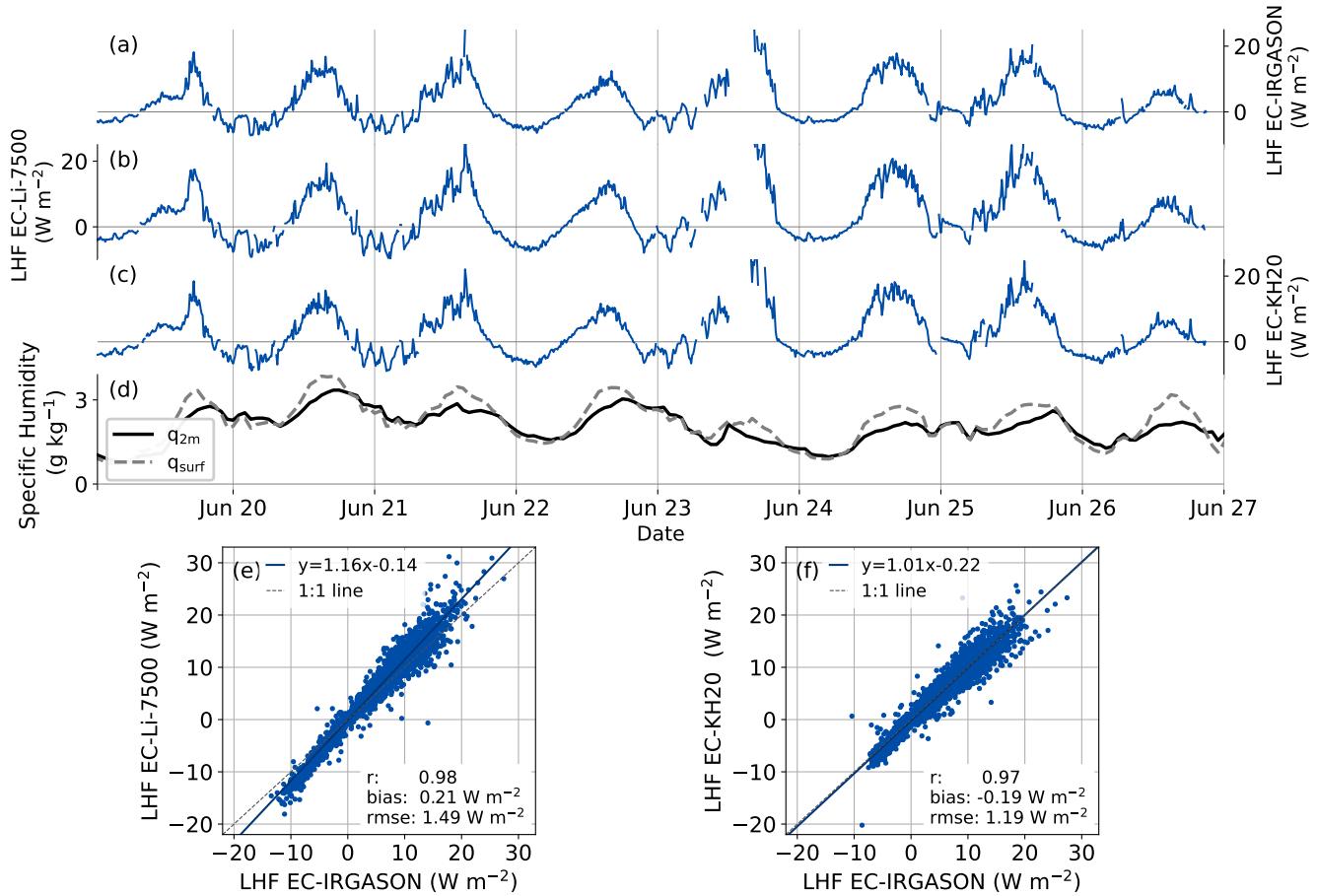
Figure 2. Examples of time series of the LHF measured by (a) the EC-IRGASON, (b) EC-Li-7500 and (c) EC-KH20 and (d) the specific humidity at 2 m and at the surface based on PROMICE AWS measurements. Direct comparisons of the LHF during the entire campaign measured by the EC-Li-7500 and EC-KH20 versus EC-IRGASON are shown in panels e and f. The EC and AWS data have a 10-minute and hourly temporal resolution, respectively.
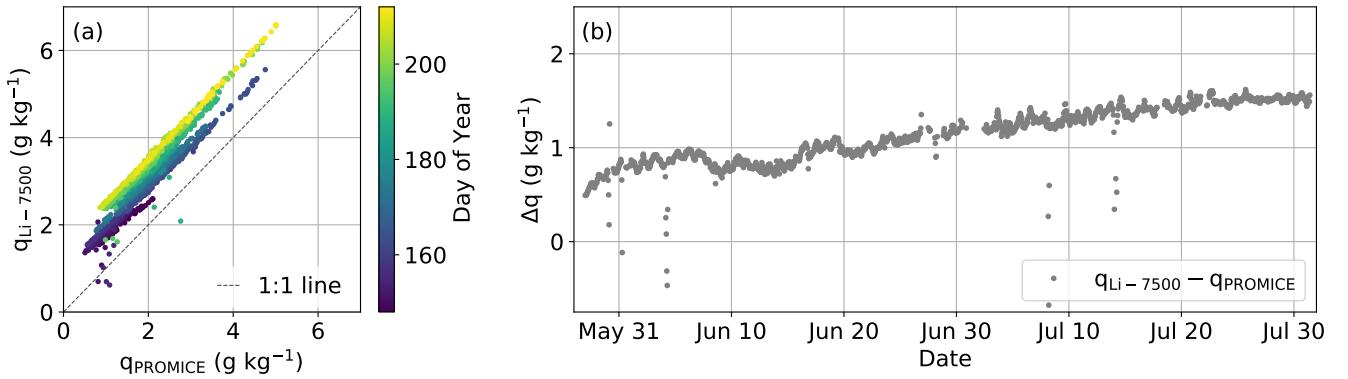
Figure 3. (a) Comparison of the hourly averaged specific humidity measured by Li-7500 and PROMICE AWS. (b) The difference between the specific humidity measured by Li-7500 and PROMICE AWS as function of time through the campaign.

bulk deposition is slightly more overestimated than bulk sublimation. Using a similar parameterisation (Andreas, 1987) for $z_{0,t}$, $z_{0,m} = 1.3 \times 10^{-4}$ m based on our EC measurements, and assuming $z_{0,q} = z_{0,t}$, improves the correspondence with the EC data (Fig. 5b and 5f), especially the SHF. However, a slightly overestimated LHF remains (slope = 1.44 and absolute
315   bias = 2.44 W m^{-2}). Using the parameterisation by Andreas (1987) no other $z_{0,m}$ value could be found that provides good fits between both calculated SHF and LHF bulk fluxes and the EC data (see Supplementary Material S6). Therefore, we use $z_{0,m} = 1.3 \times 10^{-4}$ m and $z_{0,q} = 5.7 \times 10^{-7}$ m and $z_{0,t} = 2.9 \times 10^{-4}$ m, derived from the EC measurements (see Sect. 3.2). We note that $z_{0,t}$ is larger than $z_{0,m}$ and that $z_{0,t}$ is two orders of magnitude larger than $z_{0,q}$. This is not consistent with previous findings where $z_{0,q}$ and $z_{0,t}$ are often assumed to be smaller or approximately the same as $z_{0,m}$, and $z_{0,q}$ and $z_{0,t}$ having the
320   same or nearly identical values (Van Tiggelen et al., 2023; Andreas, 1987; Smeets and Van den Broeke, 2008a). Using the above roughness lengths, we find that the bulk method provides similar LHF and SHF values as the EC-Irgason (absolute bias of 0.79 W m^{-2} and 0.67 W m^{-2}, respectively, Fig. 5c and 5g) and these values are therefore used in the rest of this study and assumed constant. It is expected that the roughness length of a snow surface varies seasonally, e.g. through higher winds in winter that promote surface snow structure change (Zuhr et al., 2021). However, as no EC measurements were conducted
325   during the winter, we only evaluate the estimated bulk fluxes during the summer (daylight) period. We assume that using the improved roughness lengths the calculated bulk fluxes provide reliable estimates during the winter as well. This is supported by a sensitivity study using roughness lengths up to one and two orders of magnitude smaller or larger than the original values (following Van Tiggelen et al., 2023), showing that the exact value of the roughness length has limited influence on the estimated flux during the winter (see Supplementary Material S7).

330   **4.3   Model comparison**

Intercomparisons between the simulated LHF from the RACMO and MAR models and observations are shown in Fig. 6. We note that there is a large spread between models and the observations in the seasonal cycle (Fig. 6a). The monthly averaged
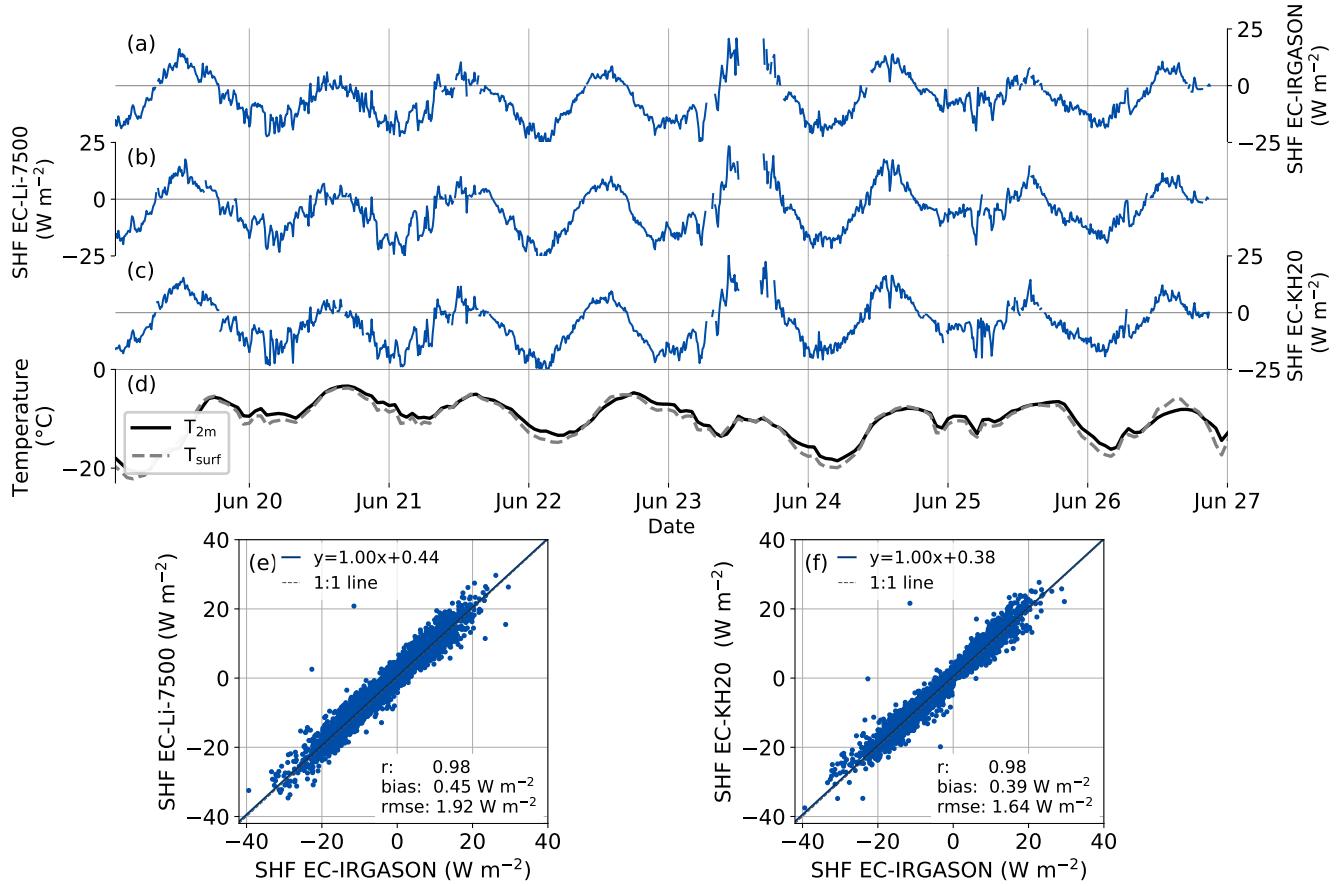
Figure 4. Examples of time series of the SHF measured by (a) the EC-IRGASON, (b) EC-Li-7500 and (c) EC-KH20 and (d) the temperature at 2 m and at the surface based on PROMICE AWS measurements. Direct comparisons of the SHF during the entire campaign measured by the EC-Li-7500 and EC-KH20 versus EC-IRGASON are shown in panels e and f. The EC and AWS data have a 10-minute and hourly temporal resolution, respectively.
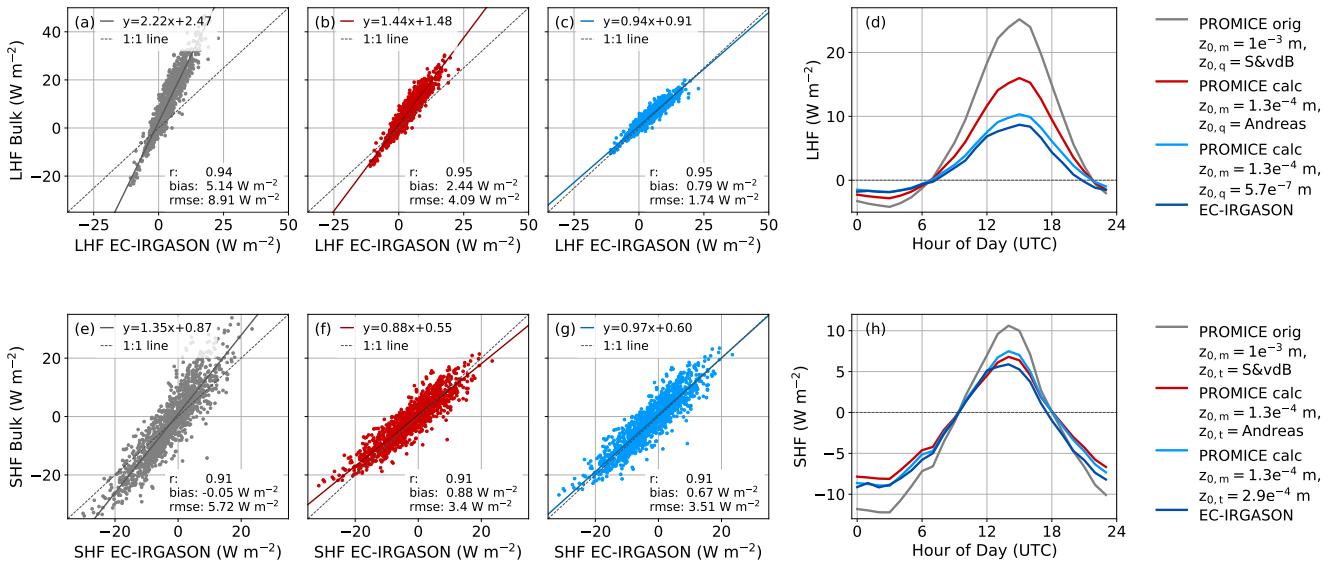
Figure 5. Comparison of the bulk flux based on the PROMICE AWS observations and EC-Irgason with the SHF in the top row and the LHF in the bottom row. Panels a and e are based on the original PROMICE data product using $z_{0,m} = 1 \times 10^{-3}$ m and $z_{0,q} = z_{0,t} = $ Smeets and Van den Broeke (2008a, b)(S&vdB). Panels b and f are the bulk fluxes recalculated using the $z_{0,m}$ from the EC-Irgason and parameterizations from Andreas (1987) shown against the observed SHF and LHF from the EC-Irgason. Panels c and d show the calculated bulk fluxes using the $z_{0,m}$, $z_{0,q}$, and $z_{0,t}$ values derived from the EC-Irgason. Panels d and h show the average diurnal cycle of the different flux calculations during the measurement campaign (28 May, 2019 to 31 July, 2019). A time series comparison of the different flux estimates is available in the Supplementary Material S8 (Fig. S7 and Fig. S8).

bulk LHF from the AWS varies between $2.6\,\mathrm{W\,m^{-2}}$ and $-0.9\,\mathrm{W\,m^{-2}}$. The difference between the monthly averaged models and observations is up to $2.1\,\mathrm{W\,m^{-2}}$ and $-1.7\,\mathrm{W\,m^{-2}}$ in June and October, respectively. Except for RACMO2.3 in summer and RACMO2.4 in June, the RCMs underestimate the LHFs year-round. Figure 6b shows the cumulative sum of the LHF over the 3.5 years of our measurements, expressed as a mass flux. While the cumulative mass flux from the AWS is approximately net zero after three complete years, simulations using MAR and RACMO2.4 result in a net deposition, with a total difference of $25\,\mathrm{mm\,w.e.}$ and $38\,\mathrm{mm\,w.e.}$, respectively. RACMO2.3 shows overestimated sublimation and a total of $-5\,\mathrm{mm\,w.e.}$ by the end of the three years. The time series in Fig. 6c shows that both the models and observations have similar diurnal cycles of the LHF in summer, although the amplitudes differ. In winter (Fig. 6d) there is a large difference between the models and the observations. MAR and RACMO2.4 episodically show strongly negative fluxes (of $-7\,\mathrm{W\,m^{-2}}$ to $-13\,\mathrm{W\,m^{-2}}$), while the bulk flux from the AWS remains close to zero (between $1\,\mathrm{W\,m^{-2}}$ and $-2\,\mathrm{W\,m^{-2}}$). RACMO2.3 shows partly opposite flux results of MAR and RACMO2.4 and simulates a positive LHF, whereas the other two simulate a negative flux.

A direct comparison between model output and observed LHF is complicated by the sublimation of drifting snow, which, when it occurs, varies strongly with height and can reach significant heights above the surface (Palm et al., 2018). In the ob-
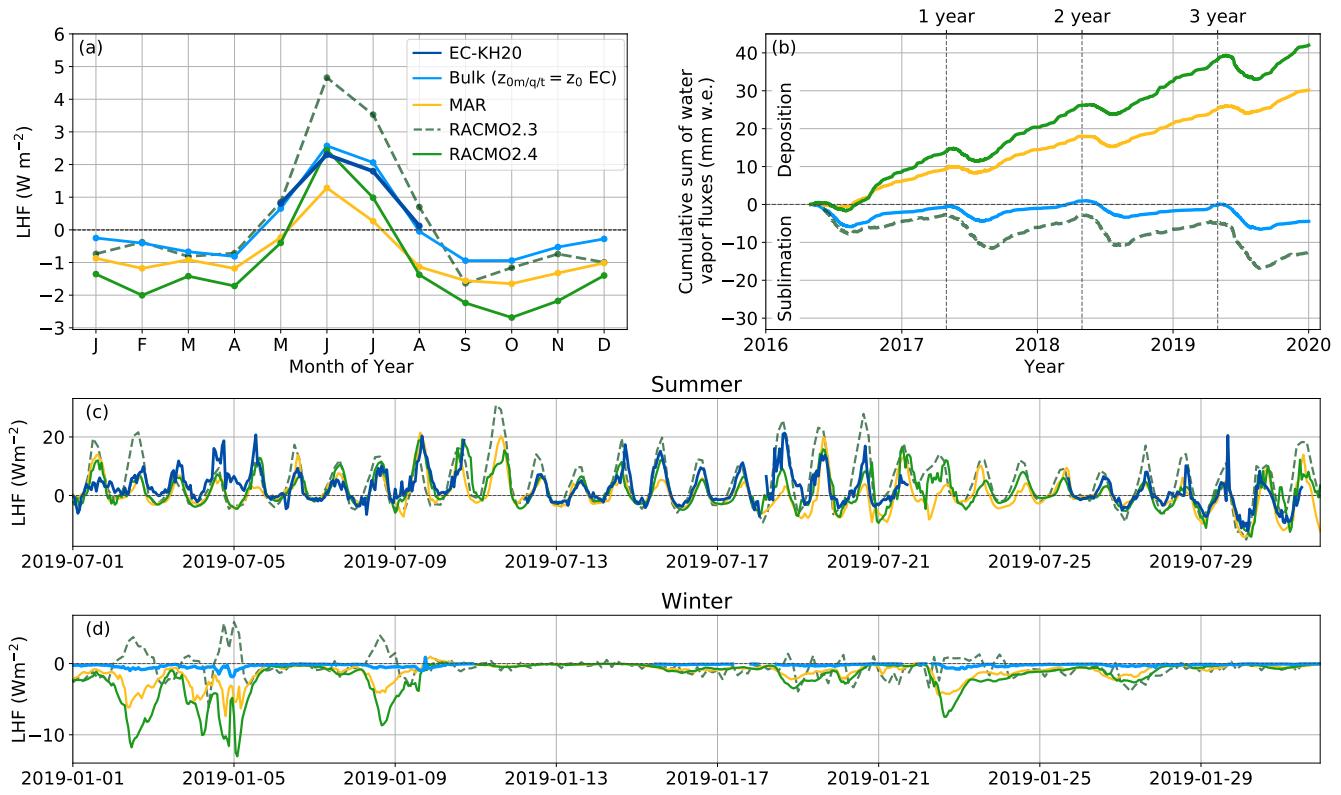
Figure 6. (a) Seasonal cycle of the LHF from May 2016 until the end of 2019. (b) Cumulative LHF expressed in mm water equivalent (mm w.e.) (note the fluxes follow the SMB sign convention in this panel). Panels c and d show examples of time series of the LHF during summer and winter, respectively. LHFs are shown based on observations from the EC-KH20 and from calculations using the bulk method using observations from the PROMICE AWS. Simulated LHFs are based on the RCM's MAR, RACMO2.3 and RACMO2.4. The observational time series from the EC-KH20 is used due to its longer available record.

servations presented here, by locally moistening and cooling the air, blowing snow sublimation would violate the constant flux assumption in the EC measurements and bulk flux calculations. RACMO2.3 has an idealised drifting snow scheme (Lenaerts et al., 2010), in which the associated vertically integrated sublimation is fully added to the surface latent heat flux, potentially explaining the overestimated sublimation in this model. In RACMO2.4 the drifting snow scheme is improved and moisture 350 from drifting snow sublimation is added directly to the associated atmospheric model layers (Gadde and Van de Berg, 2024). Given the strong vertical variations in drifting snow sublimation, here we only use the surface latent heat flux from RACMO2.4 for comparison to our observations, which may lead to underestimated sublimation. The daily drifting snow sublimation from RACMO2.4 against the PROMICE windspeed is shown in Supplementary Material S9. In MAR, the drifting snow routine was not activated for this comparison.
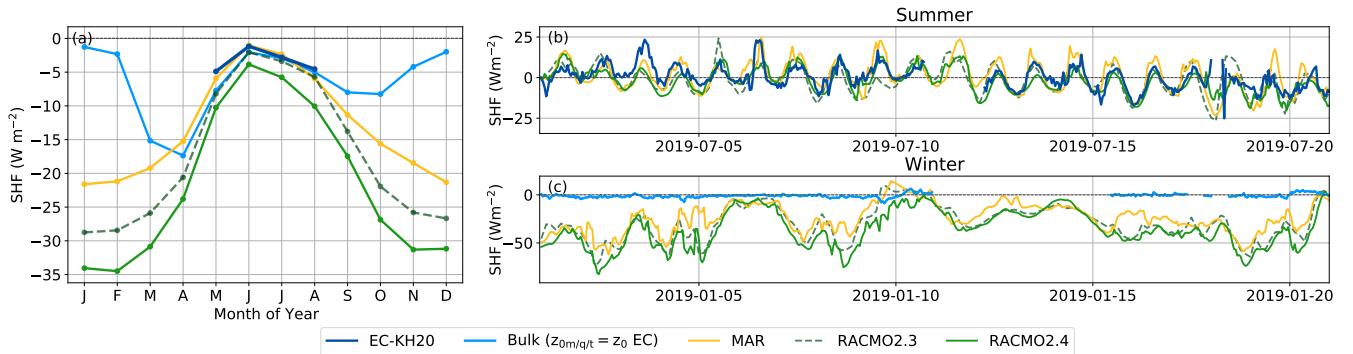
Figure 7. (a) Seasonal cycle of the SHF from May 2016 until the end of 2019. Panel b and c examples of SHF time series for a 21-day period in summer and winter, respectively. SHFs are shown based on observations from the EC-KH20 and from calculations using the bulk method using observations from the PROMICE AWS. Simulated SHFs are based on the RCM's MAR, RACMO2.3 and RACMO2.4. The observational time series from the EC-KH20 is used due to its longer available record.

355   The comparison of SHF from observations, the bulk method and the RCMs is shown in Fig. 7. When comparing the seasonal cycle based on monthly means (Fig. 7a), the models have a slightly lower to similar SHF compared to the observations in summer, but simulate considerably more negative SHF values in winter. A monthly difference between the SHF of the models and observations in winter is between -20 to $-33\,\mathrm{W\,m^{-2}}$ (Fig. 7a). The SHF time series in Fig. 7b and 7c show a similar pattern as the LHF comparison. During the summer the models and observations show similar diurnal cycles but differ in

360 amplitude and hour-to-hour variations (Fig. 7b). In winter a large difference between the SHF from the models and observations can be seen, with strongly negative hourly fluxes of up to $-62\,\mathrm{W\,m^{-2}}$ to $-86\,\mathrm{W\,m^{-2}}$ from the models and a flux close to zero ($-2\,\mathrm{W\,m^{-2}}$ to $1\,\mathrm{W\,m^{-2}}$) from the estimates from the bulk method applied to AWS data (Fig. 7c).

5   Discussion

5.1   Eddy-Covariance intercomparison

365 We compare our results from the three EC systems in the polar conditions of the Greenland Ice Sheet to the performance of similar EC systems under non-polar conditions from earlier studies. In Schmidt et al. (2012) a verified and calibrated EC system was used to validate 84 EC systems of the AmeriFlux network, which are spread out over the North American continent, hence covering a wide range of environments. They reported a relative instrumental error of $3.06 \pm 15.60\,\%$ for the SHF and $1.72 \pm 10.58\,\%$ for the LHF, for the systems using an open path gas analyser. Polonik et al. (2019) also compared different EC

370 systems, using a combination of a CSAT3A, Gill 3R-50, IRGASON and Li-7500 A, in California. For the SHF, they generally find a slope between 0.92 and 1.09, with an intercept between -0.22 and $0.92\,\mathrm{W\,m^{-2}}$ (in one case, they report an intercept of $7.17\,\mathrm{W\,m^{-2}}$) and for the LHF a slope between 0.96 and 1.07 and an intercept between $-0.2\,\mathrm{W\,m^{-2}}$ and $-0.01\,\mathrm{W\,m^{-2}}$. Mauder and Zeeman (2018) compared six different sonic anemometers, CSAT3, Gill HS-50 and R3, METEK uSonic-3 Omni,

R. M. Young 81000 and 81000RE, in southern Germany. Good agreement was found for the SHF with a slope between 0.98
and 1.02 and an intercept between 1.2 and $-2.5\,\mathrm{W\,m^{-2}}$. A comparison study by Wang et al. (2016), was carried out in a
cold desert environment in northwestern China using an IRGASON and a Windmaster Pro. They found a slope of 1.11 and an
intercept of $1.22\,\mathrm{W\,m^{-2}}$ for the SHF. Finally, a comparison study by Loescher et al. (2005) was done in Oregon, comparing
eight different sonic anemometers (a-Probe, k-Probe, CSAT3, R3, DA-600 (TR61A), SAT-550, USA-1 and RM81000), where
they found -1 to $8\,\%$ difference in the SHF.

For the cold polar conditions reported on here, we find an inter-instrument variability for the SHF with $r = 0.98$, slope $= 1.0$,
intercept $= 0.4\,\mathrm{W\,m^{-2}}$, bias between 0.4 and $0.5\,\mathrm{W\,m^{-2}}$ and an $RMSE$ between 1.6 and $1.9\,\mathrm{W\,m^{-2}}$. For the LHF is r between
0.97 and 0.98, slope between 1.01 and 1.16, intercept between -0.1 and $-0.2\,\mathrm{W\,m^{-2}}$, bias between -0.2 and $0.2\,\mathrm{W\,m^{-2}}$ and
an $RMSE$ between 1.2 and $1.5\,\mathrm{W\,m^{-2}}$. This inter-instrumental variability is consistent with the above-mentioned campaigns
in non-polar conditions. Hence, we conclude that the accuracy and precision of EC SHF and LHF measurements carried out
on the top of the Greenland Ice Sheet are comparable to EC measurements carried out under less challenging conditions. Our
measurements and their high level of correspondence provide confidence in the quality of EC systems deployed under harsh
polar conditions. However, systematic biases with the EC method, due to boundary layer characteristics in polar conditions
cannot be ruled out, such as the influence of the katabatic wind maximum, and during (sub)meso motions (Lan et al., 2022),
which both typically take place under very stable conditions and can cause the transport to deviate from a fully turbulence-
dominated regime.

5.2 Eddy-Covariance and Bulk Flux Comparison

Our comparison between the EC measurements and the SHF and LHF deduced from the bulk method confirms the generally
accepted uncertainties and challenges that come with using the bulk method in polar conditions. Known major limitations of
MOST are the underpinning assumptions, i.e. high Reynolds number flow, steady state conditions and flat homogeneous terrain,
in combination with the uncertainties in the universal functions describing the non-dimensional flux-gradient relationships
(Foken, 2006; Högström, 1988). In this study, we also highlight the strong dependence of the calculated fluxes on the value of
$z_{0,m}$ and the parameterisation used to obtain $z_{0,q}$ and $z_{0,t}$. Different roughness lengths and parameterisations can lead to strong
over- or under-estimation of the diurnal flux amplitude which has large consequences for the calculated net and total fluxes. Our
results underline that uncertainty from using the bulk method can be greatly reduced by having a period of combined AWS and
EC measurements in which not only $z_{0,m}$ is determined but also the fluxes are directly compared. Further improvement of the
accuracy of the bulk method might be achieved by also having EC measurement during winter, making year-round evaluation
of the roughness length possible.

The two orders of magnitude difference between the derived $z_{0,t}$ and $z_{0,q}$ explain the different accuracy of the bulk LHF
and SHF when it is assumed that $z_{0,q} = z_{0,t}$ (Fig. 5abef). Comparing a filtered selection of all the measured $z_{0,t}$ and $z_{0,q}$ values
during our campaign with different parameterizations shows that the measured $z_{0,t}$ is consistently higher than the parameterised
$z_{0,t}$ and the measured $z_{0,q}$ is consistently lower than $z_{0,t}$ (Appendix B, Fig. B2). We note that the calculation of the roughness
lengths is based on MOST and the accuracy of the temperature and humidity gradient measured by the PROMICE AWS. Our

result implies that the parameterisation for $z_{0,t}$ and the common assumption that $z_{0,t}$ is equal to $z_{0,q}$, which is used in most models and datasets, might not be valid over the entire Greenland Ice Sheet.

5.3 Caveats related to the PROMICE data during winter

There is a large difference between the wintertime SHF/LHF values simulated by the RCMs and the bulk flux calculations (Fig. 6 and Fig. 7). It is not possible to reconcile those discrepancies within the measurement uncertainties and hence this indicates either large systematic biases in models, issues with the measurements, assumptions related to the measurements or a combination of those. Intercomparison of the independent $2\,\mathrm{m}$ temperature and wind speed measured by the PROMICE and GC-Net AWS show similar characteristics. During Arctic winter, conditions are mostly quasi-saturated, resulting in the specific humidity predominantly being dependent on air temperature, and the uncertainty in the relative humidity is unlikely to have a significant impact on the fluxes. The most important observational uncertainty is therefore that of the surface temperature, which is derived from the measured upward longwave radiation. This is especially important since the surface temperature is key for determining the near-surface temperature gradient, which determines the difference between flux results from the model simulation and observations (see Sect. 5.4 and Fig. 9). We note that the net longwave radiation is close to zero for long periods spanning several days to over a week (Fig. 8a). The near-zero net longwave radiation sometimes coincides with low temperatures ($T < -50\,^{\circ}\mathrm{C}$), conditions normally associated with a surface based temperature inversion rooted in longwave radiative cooling (Van den Broeke et al., 2004; Miller et al., 2017). Times when $T < -50\,^{\circ}\mathrm{C}$ are therefore also removed from the data (Sect 2.3). While we are observing near zero net long wave radiation, it is important to note that a zero net longwave radiation could also be explained by frosting of the sensor, which leads to artificial neutral conditions and SHF/LHF values close to zero (Fig. 8b). Measurements from both Summit in Greenland (Miller et al., 2013; Berkelhammer et al., 2016), the katabatic wind zone in Antarctica (Van den Broeke et al., 2005a, 2009) and modelling studies (Shahi et al., 2020) show that neutral conditions are uncommon during winter time. To explore whether frosting obstructs the radiation sensor, we compare the near-surface temperature gradient estimated from the PROMICE AWS with the near-surface air temperature gradient obtained from the two independent GC-NET AWS temperature measurements installed at two different heights (Fig. 8e and 8f). One can notice two important findings: 1) The independently observed temperature gradients by the single-level PROMICE and two-level GC-NET AWS are generally approximately similar and an order of magnitude smaller than the modelled temperature gradient (see Fig. 9i and Fig. 10 for all winter months). 2) Features in the synoptic-scale variability of the near-surface temperature gradient are observable in both AWS datasets (see Supplementary Material S10, Fig. S10 to S15 for other winter months).

A second line of evidence supporting the radiation sensor measurements can be deduced from the shallow near-surface ($10\,\mathrm{cm}$) snow temperature, which is less prone to measurement uncertainties (Fig. 8c and 8d). Due to the thermal mass of the snow, it is not to be expected that the magnitude of the temperature gradient deduced from the near-surface snowpack temperature ($T_{2.6} - T_{\mathrm{Snow}}$, Fig. 8d) is equivalent to the temperature gradient deduced from the snow skin surface ($T_{2.6} - T_{\mathrm{Surf}}$, Fig. 8e). However, we note the general good agreement in the evolution of the sign of the temperature gradient based on the snowpack ($T_{2.6} - T_{\mathrm{Snow}}$) and skin surface temperature ($T_{2.6} - T_{\mathrm{Surf}}$). For example, when colder air is present, the air temperature

is lower than the snow surface (e.g. 10th to 15th of January 2019) and vice-versa (e.g. 1st to 10th of January). Interpretation is, however, not straightforward, as the thermal inertia of the snowpack leads to a delayed response to surface forcing, and snow temperature reflects a delayed and smoothened pattern of the air temperature, reflecting a mixture of heat exchange between air, surface and subsurface at longer time scales.

Altogether, based on our assessment of observations and models, we cannot decide with strong certainty whether modelled or observed wintertime SHF/LHF values are closer to reality, and any conclusions based on either data source should be drawn with care. The large model-data discrepancy and our discussion here illustrate the outstanding requirement to resolve this question for areas with wintertime conditions such as the EastGRIP location, and the need for more direct observations of the near-surface temperature gradient.
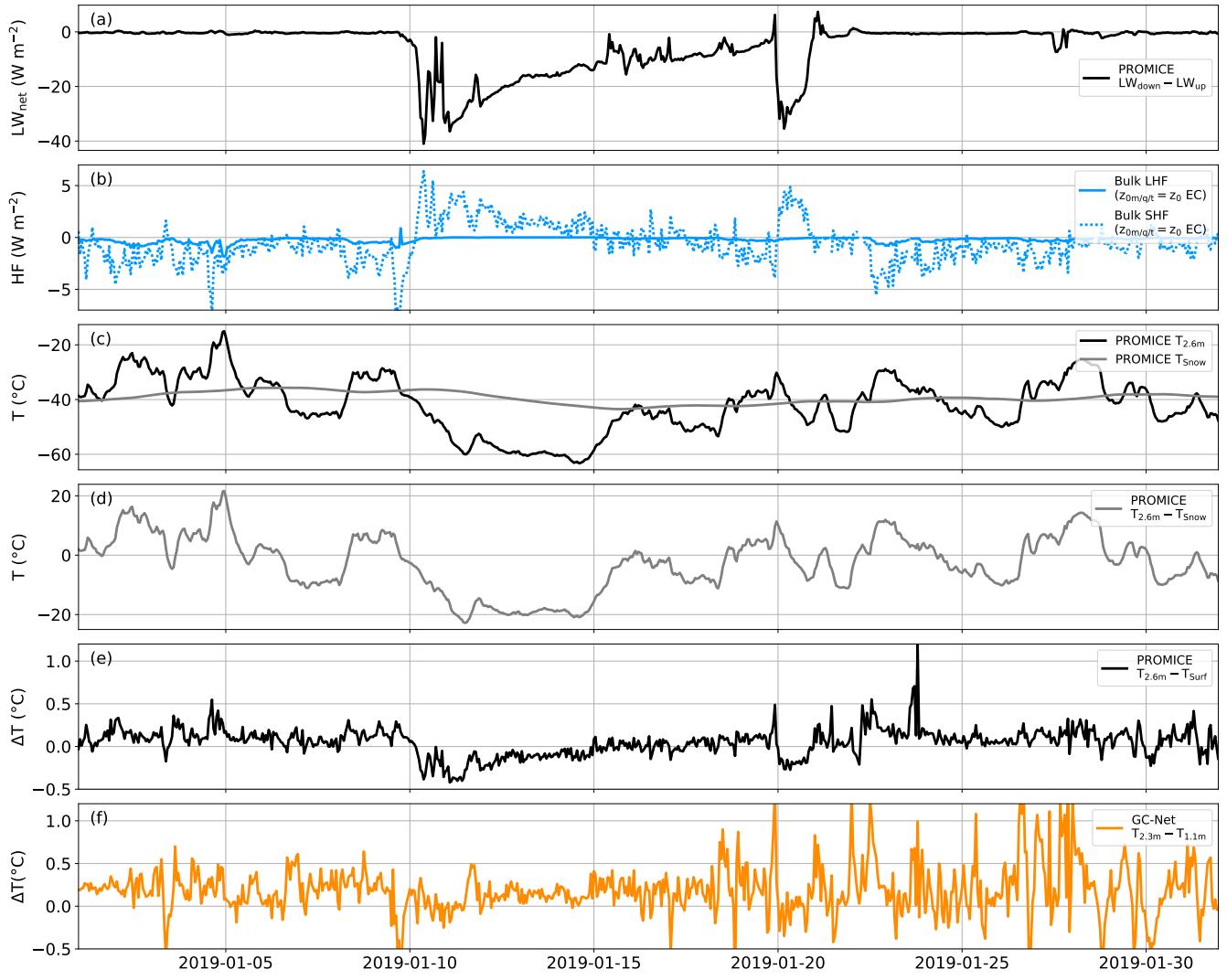
Figure 8. Time series of winter AWS observations with (a) the net longwave radiation, (b) the calculated sensible and latent heat flux, using the $z_{0,m}$, $z_{0,q}$ and $z_{0,t}$ values derived from the EC-Irgason, (c) the air temperature at $2.6\,\mathrm{m}$ above the surface and the snow temperature approximately $10\,\mathrm{cm}$ below the surface, (d) the temperature difference between the $2.6\,\mathrm{m}$ and snow temperature and (e) the PROMICE temperature difference between $2.6\,\mathrm{m}$ and the surface, determined via the longwave radiation and (f) the GC-Net temperature difference between $2.3\,\mathrm{m}$ and $1.1\,\mathrm{m}$. Note that the complete dataset is shown for this figure, including the data below $-50\,^{\circ}\mathrm{C}$. Comparison of the PROMICE AWS and model temperature gradients is analysed in Fig. 9. Separate up- and downward longwave radiation and a magnified view of the near-zero variability of the net longwave radiation are provided in Supplementary Material S11.

5.4 Observations and models comparison

Assuming that observational uncertainty cannot fully explain the difference with the modelled fluxes during winter, we explore potential shortcomings in the model simulations of either the air temperature or the snow surface temperature. The time series in Fig. 9 of the LHF, SHF and driving variables (seasonal cycle provided in Supplementary Material S12) show that, while the wind speed in all three models is similar to the observed wind speed, both the humidity and temperature gradient are much larger than the observations. This means that the larger modelled magnitudes of LHF and SHF in winter result from a larger near-surface temperature gradient and therefore also a larger humidity gradient in the models. Since EastGRIP is located centrally in the modelling domain of both MAR and RACMO, we assume the impact of ERA5 forcing at the lateral boundaries to be small. With the tentative assumption that the observed surface temperatures are correct, the evaluated climate models simulate a too strong stability in this part of the ice sheet during winter. This is supported by a comparison of the near-surface temperature gradient measured by both the PROMICE and the two-level GC-Net AWS and the three RCMs over all winter months (see Fig. 10). The too strong stability in the models implies that the processes driving the surface gradients are not yet accurately modelled and parameterised. This persistently larger near-surface temperature gradient during winter can have a considerable impact, as the LHF and SHF are important for obtaining an accurate SMB and closing the SEB. As seen in Fig. 6b small differences in LHF estimates can lead to large differences on longer timescales. Although studies suggest that the contribution of the LHF might switch to net mass loss in the future (Cullen et al., 2014), most RCMs simulate the LHF to be a positive contributor to the SMB to date. In fact, by correcting the MAR model with summer observations at EastGRIP, Dietrich et al. (2024) find the LHF to be a negative SMB contributor in their simulations. They propose that the difference in LHF between the model and observations during summer arises from a negative bias in downwelling longwave radiation, as also found by Fettweis et al. (2017), from the cloud scheme, while the winter bias may be caused by vertical mixing through katabatic winds that is not represented in the model (Dietrich et al., 2024). Similar to Dietrich et al. (2024), we find that RACMO in winter also overestimates deposition compared to AWS observations at EastGRIP, probably a result of too low surface temperatures caused by a negative bias in incoming longwave radiation (Van Dalum et al., 2024). This raises the important question of whether both established RCMs face systematic errors in the representation of the surface boundary layer on ice sheets during winter. Besides their importance for obtaining an accurate SEB and SMB, which are used for sea level rise estimates, accurately simulating surface fluxes is also important for other fields of study such as the interpretation of water isotope climate proxies from the snowpack and ice cores (Wahl et al., 2022; Dietrich et al., 2023). Underscoring the need for better knowledge and model representation of the surface near-stability during winter on the Greenland Ice Sheet, both by improving model parameterisations and increasing the number of observations. This includes obtaining direct observations of the surface temperature, but also observations of blowing snow, to better understand and parameterise the impact of blowing snow sublimation on the heat fluxes.
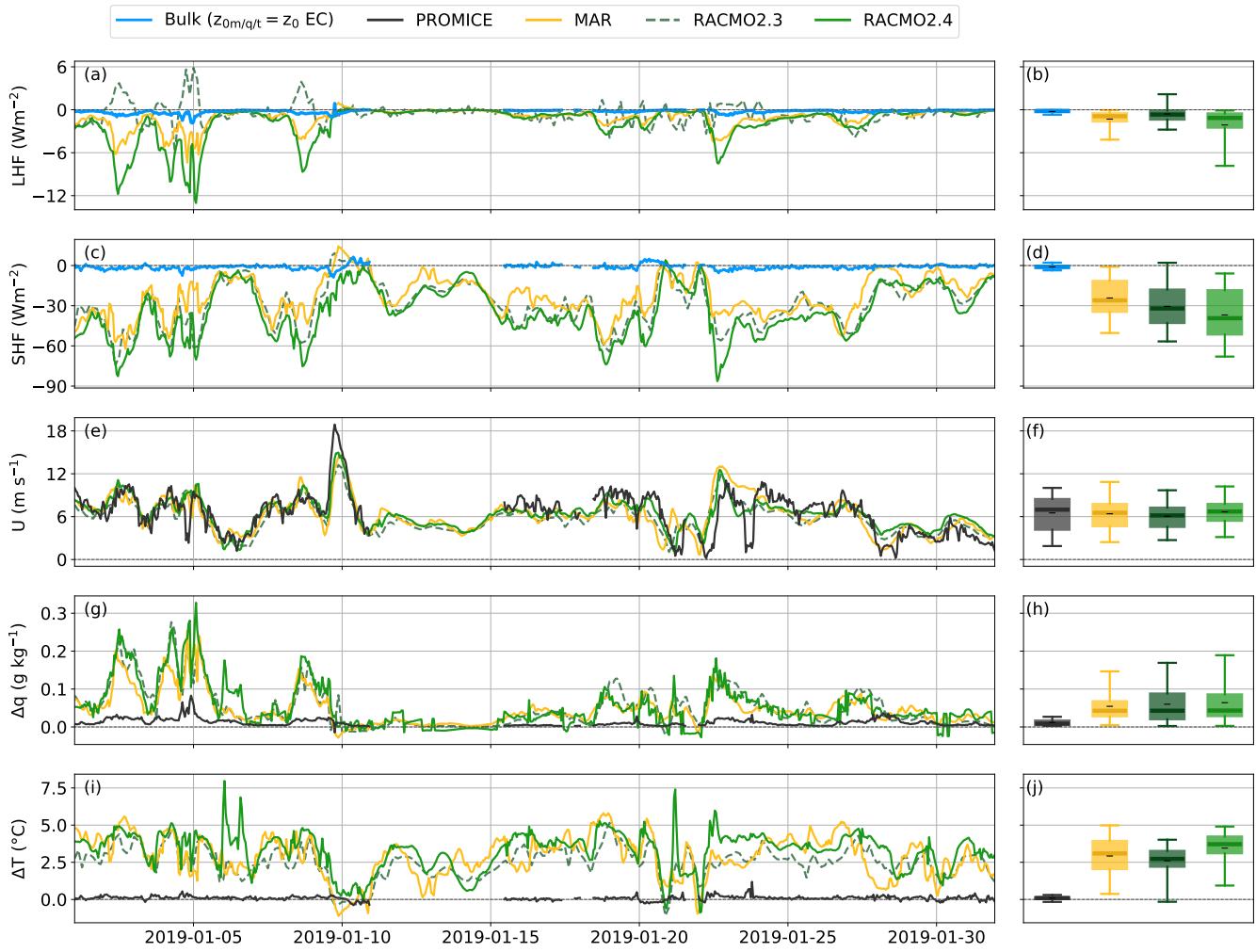
Figure 9. Examples of winter time series showing (a) the SHF, (c) LHF, (e) windspeed, (g) specific humidity difference between 2 m and surface level and (i) temperature difference between 2 m and surface level. Panels b, d, f, h and j show boxplots over the same period, where the whiskers indicate the 5th-95th percentile, the box the 25th to 50th percentile, the thick line the median and the black dash (-) the mean.
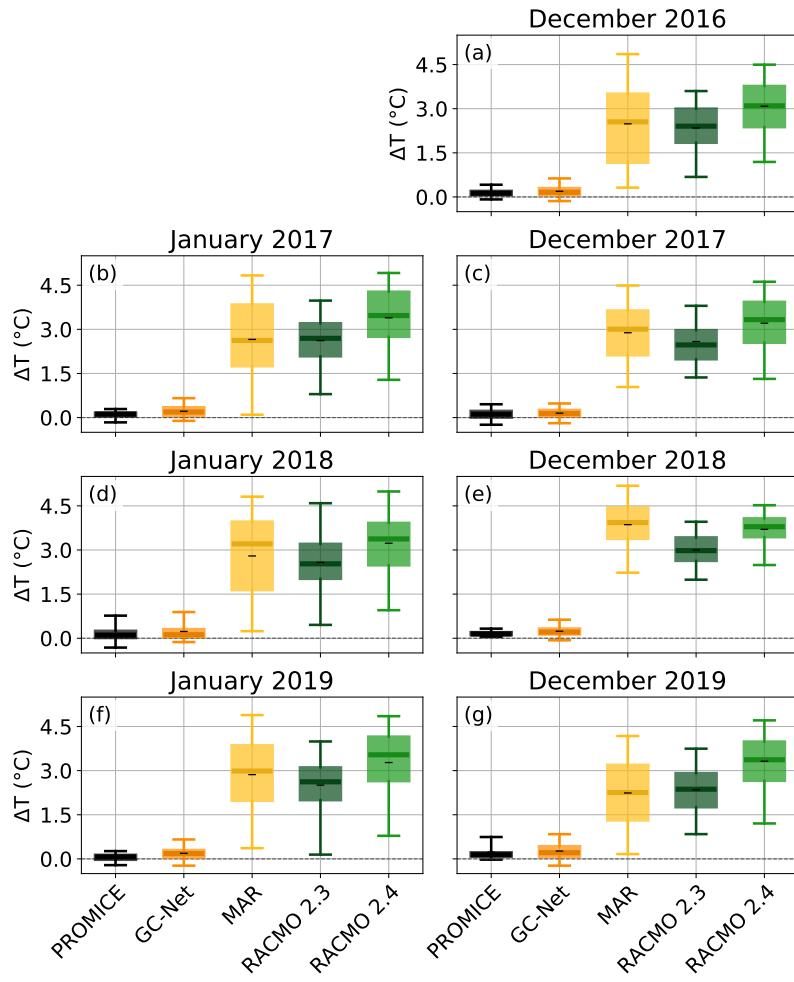
Figure 10. Boxplots of the near-surface atmospheric temperature gradients of the winter months from the PROMICE and GC-Net AWS and the three RCMs MAR, RACMO 2.3 and RACMO 2.4. The whiskers of the boxplots indicate the 5th-95th percentile, the box the 25th to 75th percentile, the thick line the median and the black dash (-) the mean. Note that the temperature gradients of the PROMICE AWS and the three RCMs are between 2 m and the surface, while the GC-Net is between two air temperature sensors spaced 1.3 m apart, with the lowest approximately 1 to 2 m above the surface.

6   Conclusions

An instrument intercomparison of three co-located EC systems in the interior of the Greenland Ice Sheet shows that the EC method provides accurate LHF and SHF measurements during summer on the ice sheet. This is based on the high levels of correspondence of the measured fluxes by the three EC systems. Differences in the fluxes measured by the individual systems can be explained by instrumental error, as is the case for the LHF measured by the EC-Li-7500 in our study, or otherwise, fall

into the uncertainty range documented by other EC comparison studies in non-polar conditions. Comparing the validated EC fluxes with fluxes obtained using the bulk method illustrates the caveats of the bulk method. Besides already known issues, like limitations of MOST, this study highlights the dependence of the flux calculation on the value of $z_{0,m}$ and the limitation
490 of parameterisations for obtaining $z_{0,q}$ and $z_{0,t}$. Specifically, using a fixed roughness length over the ice sheet introduces a large bias in the bulk flux measurement compared to EC measurements, and the often-used assumption that $z_{0,q}$ and $z_{0,t}$ are equal does not seem to hold in this location. Therefore, this study highlights the need for year-round EC measurements in the centre of the ice sheet, to improve both existing bulk flux estimates and roughness length parameterisations. Lastly, comparison of observations with RCMs MAR, RACMO2.3 and RACMO2.4 shows large differences between the simulated and observed
495 LHF and SHF, especially during winter. Our results indicate that the winter difference comes from a consistent overestimation of the atmospheric stability at EastGRIP in climate models, but observational uncertainty due to frosting cannot be ruled out and further measurements are needed to support these results. Too strong near-surface gradients during winter in the models result in persistently larger turbulent exchange, leading to errors in the contribution of the LHF to the SMB of the ice sheet and both the LHF and SHF to the SEB. Contemporary and future SMB estimates based solely on models might thus be less
500 certain than previously thought, underlining the need for improving model parameterisations and obtaining more and reliable observations on the Greenland Ice Sheet in particular and polar regions in general.

Data availability. The raw EC-KH20, EC-IRGASON, and EC-Li-7500 data from the summer of 2019 are available on Pangaea: https:// doi.pangaea.de/10.1594/PANGAEA.982997, Steen-Larsen et al. (2025d), https://doi.pangaea.de/10.1594/PANGAEA.931439, Steen-Larsen and Wahl (2021), https://doi.pangaea.de/10.1594/PANGAEA.982996, Steen-Larsen et al. (2025e). The processed fluxes from the EC-KH20,
505 EC-IRGASON and EC-Li-7500 are available on Pangaea: https://doi.pangaea.de/10.1594/PANGAEA.983056, Steen-Larsen et al. (2025b), https://doi.pangaea.de/10.1594/PANGAEA.983054,Steen-Larsen et al. (2025a), https://doi.pangaea.de/10.1594/PANGAEA.983057, Steen-Larsen et al. (2025c). EC-KH20 data from the summers of 2016, 2017, 2018 is available on Pangaea (https://doi.pangaea.de/10.1594/ PANGAEA.962310, Steen-Larsen et al. (a), https://doi.pangaea.de/10.1594/PANGAEA.962311, Steen-Larsen et al. (b), https://doi.org/10. 1594/PANGAEA.946741, Steen-Larsen et al. (2022)). The PROMICE AWS product is available at https://doi.org/10.22008/FK2/IW73UU
510 (How et al., 2022). The GC-Net data is available at https://doi.org/10.22008/FK2/VVXGUT (Steffen et al., 2022). The MAR simulations are available on Zenodo (https://doi.org/10.5281/zenodo.8335402, Dietrich (2023)). The three-hourly RACMO2.3p2 and hourly RACMO2.4p1 time series from 2010 to 2020 from the grid cell closest to EastGRIP are available on Zenodo (https://doi.org/10.5281/zenodo.14930860, Haven et al., 2025).

Appendix A

515 Equation A1 shows the Andreas (1987) parameterisation of the roughness length for moisture and heat. The values for coefficients b_0, b_1 and b_2 are provided in table A1 and $R_* = u_* z_0 / v$ is the roughness Reynolds number.

$$\ln\left(z_s/z_0\right) = b_0 + b_1 \ln R_* + b_2 \left(\ln R_*\right)^2 \tag{A1}$$

	$R_* \leq 0.135$	$0.135 < R_* < 2.5$	$2.5 \leq R_* \leq 1000$
Temperature			
b_0	1.250	0.149	0.317
b_1	-	-0.550	-0.565
b_2	-	-	-0.183
Water vapor			
b_0	1.610	0.351	0.396
b_1	-	-0.628	-0.512
b_2	-	-	-0.180

Table A1. Table adapted from Andreas (1987): Values of the coefficients in Equation A1

Appendix B

An overview of the roughness length values for momentum, moisture and heat measured during the campaign, filtered for neutral conditions (-0.02 $< z/L <$ 0.02) and for $z_{0,m}$ for sufficient wind ($U > 3\,\mathrm{m\,s^{-1}}$), is shown in Fig. B1.
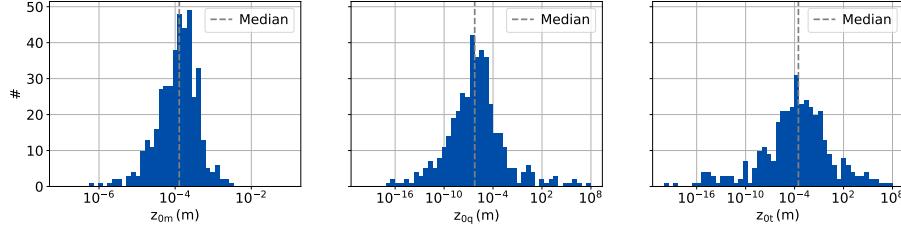
Figure B1. Histograms of the hourly roughness length values derived from the EC-IRGASON and PROMICE AWS observations.

A comparison of the roughness length values obtained from the EC-IRGASON and different roughness length parameterisations is provided in Fig. B2. To limit noise, the following selection is applied to the roughness length values displayed in Fig. B2: $U > 3\,\mathrm{m\,s^{-1}}$, $|q_{2m} - q_{surf}| > 0.1\,\mathrm{g\,kg^{-1}}$, $|t_{2m} - t_{surf}| > 0.5\,°\mathrm{C}$, $|z/L| < 0.2$, $1 < \sqrt{w}/u_* < 1.5$ and $0.1\,\mathrm{m\,s^{-1}} < |u_*| < 1.5\,\mathrm{m\,s^{-1}}$.

Author contributions. IH wrote the initial draft with contributions from all authors. The study conceptualization were carried out by HCSL, JR, SW, and IH. Formal analysis was carried out by IH and LJD with support from STK, MvT, SW, and HCSL. Methodology was developed by HCSL and SW. IH was supervised by HCSL, JR, MvdB, and MvT. Model simulations were provided by LJD, MvdB, and MvT. Instrumental resources were provided by JR, AH, JEB. Funding acquisition and project administration was done by HCSL.
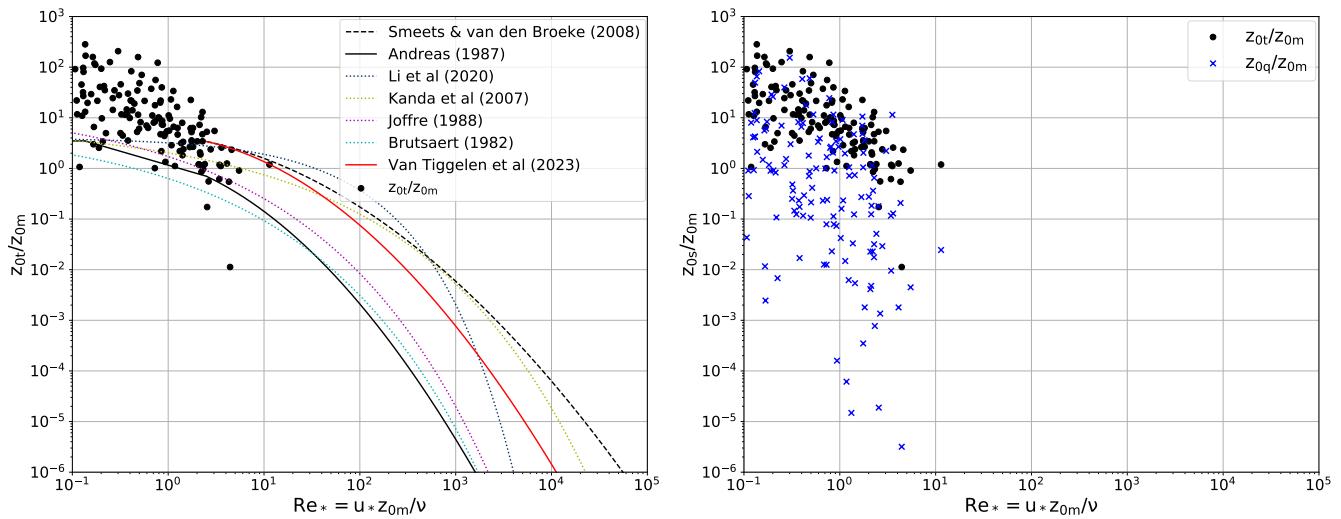
Figure B2. The hourly ratio of $z_{0,t}/z_{0,m}$ from the EC-IRGASON and PROMICE AWS observations against the roughness Reynolds number $Re_* = u_* z_{0,m}/v$. Plotted together with (a) lines denoting the parameterisation from Smeets and Van den Broeke (2008b), Andreas (1987), Li et al. (2020), Kanda et al. (2007), Joffre (1988), Brutsaert (1982) and Van Tiggelen et al. (2023) and (b) the hourly $z_{0,q}/z_{0,m}$ ratio from the EC-IRGASON and PROMICE AWS observations. The EC-IRGASON values are hourly averages of the 10-minute covariances.

Competing interests. At least one of the (co-)authors is a member of the editorial board of The Cryosphere.

Financial support. This research has been supported by the European Research Council, the European Union's H2020 program (SNOWISO, grant no. 759526)

Acknowledgements. This paper is a contribution to the H2020 European Research Council Starting Grant project SNOWISO (grant agreement no. 759526). EGRIP is directed and organized by the Centre for Ice and Climate at the Niels Bohr Institute, University of Copenhagen. It is supported by funding agencies and institutions in Denmark (A. P. Møller Foundation, University of Copenhagen), USA (US National Science Foundation, Office of Polar Programs), Germany (Alfred Wegener Institute, Helmholtz Centre for Polar and Marine Research), Japan (National Institute of Polar Research and Arctic Challenge for Sustainability), Norway (University of Bergen and Trond Mohn Foundation), Switzerland (Swiss National Science Foundation), France (French Polar Institute Paul-Emile Victor, Institute for Geosciences and Environmental research), Canada (University of Manitoba) and China (Chinese Academy of Sciences and Beijing Normal University). Data from the Programme for Monitoring of the Greenland Ice Sheet (PROMICE) are provided by the Geological Survey of Denmark and Greenland (GEUS) at http://www.promice.dk. Data analysis and model simulations were performed on resources provided by Sigma2 – the National Infrastructure for High Performance Computing and Data Storage in Norway. SW acknowledges funding from the Research Council of Norway (335140). AH acknowledges funding from UArctic Chair and from the Research Council of Norway (332635 & 342265), the Re-

search Council of Finland (363970), and the Fulbright Commission. We want to thank Christiaan van Dalum for providing the data from RACMO2.4p1. We want to thank Alexandra Zuhr and Hanna Meyer for servicing the EC systems during the field campaign.

545 References

Andreas, E. L.: A theory for the scalar roughness and the scalar transfer coefficients over snow and sea ice, Boundary-Layer Meteorology, 38, 159–184, https://doi.org/10.1007/BF00121562, 1987.

Aschwanden, A., Fahnestock, M. A., Truffer, M., Brinkerhoff, D. J., Hock, R., Khroulev, C., Mottram, R., and Khan, S. A.: Contribution of the Greenland Ice Sheet to sea level over the next millennium, Science Advances, 5, eaav9396, https://doi.org/10.1126/sciadv.aav9396, 550   2019.

Berkelhammer, M., Noone, D. C., Steen-Larsen, H. C., Bailey, A., Cox, C. J., O'Neill, M. S., Schneider, D., Steffen, K., and White, J. W. C.: Surface-atmosphere decoupling limits accumulation at Summit, Greenland, Science Advances, 2, https://doi.org/10.1126/sciadv.1501704, 2016.

Box, J. E. and Steffen, K.: Sublimation on the Greenland Ice Sheet from automated weather station observations, Journal of Geophysical 555   Research: Atmospheres, 106, 33 965–33 981, https://doi.org/https://doi.org/10.1029/2001JD900219, 2001.

Brutsaert, W.: Evaporation into the Atmosphere; Theory, History and Applications, Springer Netherlands, 1st edn., ISBN 9789401714976, https://doi.org/10.1007/978-94-017-1497-6, 1982.

Cullen, N. J. and Steffen, K.: Unstable near-surface boundary conditions in summer on top of the Greenland Ice Sheet, Geophysical Research Letters, 28, 4491–4493, https://doi.org/https://doi.org/10.1029/2001GL013417, 2001.

560 Cullen, N. J., Steffen, K., and Blanken, P. D.: Nonstationarity of turbulent heat fluxes at Summit, Greenland, Boundary-Layer Meteorology, 122, 439–455, https://doi.org/10.1007/s10546-006-9112-2, 2007.

Cullen, N. J., Mölg, T., Conway, J., and Steffen, K.: Assessing the role of sublimation in the dry snow zone of the Greenland ice sheet in a warming world, Journal of Geophysical Research: Atmospheres, 119, 6563–6577, https://doi.org/10.1002/2014JD021557, 2014.

Dietrich, L. J.: MAR model simulations 1990-2020 for the EastGRIP drilling site in Greenland, https://doi.org/10.5281/zenodo.8335402, 565   type: dataset, 2023.

Dietrich, L. J., Steen-Larsen, H. C., Wahl, S., Jones, T. R., Town, M. S., and Werner, M.: Snow-Atmosphere Humidity Exchange at the Ice Sheet Surface Alters Annual Mean Climate Signals in Ice Core Records, Geophysical Research Letters, 50, e2023GL104 249, https://doi.org/10.1029/2023GL104249, 2023.

Dietrich, L. J., Steen-Larsen, H. C., Wahl, S., Faber, A.-K., and Fettweis, X.: On the importance of the humidity flux for the surface mass 570   balance in the accumulation zone of the Greenland Ice Sheet, The Cryosphere, 18, 289–305, https://doi.org/10.5194/tc-18-289-2024, 2024.

Ettema, J., Van den Broeke, M. R., Van Meijgaard, E., and Van de Berg, W. J.: Climate of the Greenland ice sheet using a high-resolution climate model – Part 2: Near-surface climate and energy balance, The Cryosphere, 4, 529–544, https://doi.org/10.5194/tc-4-529-2010, 2010.

Fausto, R. S., Van As, D., Mankoff, K. D., Vandecrux, B., Citterio, M., Ahlstrøm, A. P., Andersen, S. B., Colgan, W., Karlsson, N. B., 575   Kjeldsen, K. K., Korsgaard, N. J., Larsen, S. H., Nielsen, S., Pedersen, A. Ø., Shields, C. L., Solgaard, A. M., and Box, J. E.: Programme for Monitoring of the Greenland Ice Sheet (PROMICE) automatic weather station data, Earth System Science Data, 13, 3819–3845, https://doi.org/10.5194/essd-13-3819-2021, 2021.

Fettweis, X., Box, J. E., Agosta, C., Amory, C., Kittel, C., Lang, C., Van As, D., Machguth, H., and Gallée, H.: Reconstructions of the 1900–2015 Greenland ice sheet surface mass balance using the regional climate MAR model, The Cryosphere, 11, 1015–1033, 580   https://doi.org/10.5194/tc-11-1015-2017, 2017.

Foken, T.: 50 Years of the Monin–Obukhov Similarity Theory, Boundary-Layer Meteorology, 119, 431–447, https://doi.org/10.1007/s10546-006-9048-6, 2006.

Fox-Kemper, B., Hewitt, H., Xiao, C., Aðalgeirsdóttir, G., Drijfhout, S., Edwards, T., Golledge, N., Hemer, M., Kopp, R., Krinner, G., Mix, A., Notz, D., Nowicki, S., Nurhati, I., Ruiz, L., Sallée, J.-B., Slangen, A., and Yu, Y.: Ocean, Cryosphere and Sea Level Change, in: Climate Change 2021: The Physical Science Basis. Contribution of Working Group I to the Sixth Assessment Report of the Intergovernmental Panel on Climate Change, edited by Masson-Delmotte, V., Zhai, P., Pirani, A., Connors, S., Péan, C., Berger, S., Caud, N., Chen, Y., Goldfarb, L., Gomis, M., Huang, M., Leitzell, K., Lonnoy, E., Matthews, J., Maycock, T., Waterfield, T., Yelekçi, O., Yu, R., and Zhou, B., pp. 1211–1362, Cambridge University Press, Cambridge, United Kingdom and New York, NY, USA, https://doi.org/10.1017/9781009157896.011, 2021.

Gadde, S. and Van de Berg, W. J.: Contribution of blowing-snow sublimation to the surface mass balance of Antarctica, The Cryosphere, 18, 4933–4953, https://doi.org/10.5194/tc-18-4933-2024, 2024.

Grachev, A. A., Fairall, C. W., Persson, P. O. G., Andreas, E. L., and Guest, P. S.: Stable Boundary-Layer Scaling Regimes: The Sheba Data, Boundary-Layer Meteorology, 116, 201–235, https://doi.org/10.1007/s10546-004-2729-0, 2005.

Haven, I., Steen-Larsen, H. C., Dietrich, L. J., Wahl, S., Box, J., Van den Broeke, M. R., Hubbard, A., Kral, S., Reuder, J., and Van Tiggelen, M.: RACMO2.3p2 and RACMO2.4p1 model timeseries 2011-2021 for the EastGRIP drilling site in Greenland, https://doi.org/10.5281/zenodo.14930860, 2025.

Holtslag, B. and De Bruin, H.: Applied Modeling of the Nighttime Surface Energy Balance over Land, Journal of Applied Meteorology, 27, 689–704, https://doi.org/10.1175/1520-0450(1988)027<0689:AMOTNS>2.0.CO;2, 1988.

How, P., Abermann, J., Ahlstrøm, A., Andersen, S., Box, J. E., Citterio, M., Colgan, W., Fausto., R., Karlsson, N., Jakobsen, J., Langley, K., Larsen, S., Lund, M., Mankoff, K., Pedersen, A., Rutishauser, A., Shield, C., Solgaard, A., Van As, D., Vandecrux, B., and Wright, P.: PROMICE and GC-Net automated weather station data in Greenland, https://doi.org/10.22008/FK2/IW73UU, 2022.

Högström, U.: Non-dimensional wind and temperature profiles in the atmospheric surface layer: A re-evaluation, Boundary-Layer Meteorology, 42, 55–78, https://doi.org/10.1007/BF00119875, 1988.

Joffre, S. M.: Modelling the dry deposition velocity of highly soluble gases to the sea surface, Atmospheric Environment (1967), 22, 1137–1146, https://doi.org/10.1016/0004-6981(88)90343-5, 1988.

Kaimal, J. C., Wyngaard, J. C., Izumi, Y., and Coté, O. R.: Spectral characteristics of surface-layer turbulence, Quarterly Journal of the Royal Meteorological Society, 98, 563–589, https://doi.org/https://doi.org/10.1002/qj.49709841707, 1972.

Kanda, M., Kanega, M., Kawai, T., Moriwaki, R., and Sugawara, H.: Roughness Lengths for Momentum and Heat Derived from Outdoor Urban Scale Models, Journal of Applied Meteorology and Climatology, 46, 1067–1079, https://doi.org/10.1175/jam2500.1, 2007.

Lan, C., Liu, H., Katul, G. G., Li, D., and Finn, D.: Turbulence Structures in the Very Stable Boundary Layer Under the Influence of Wind Profile Distortion, Journal of Geophysical Research: Atmospheres, 127, e2022JD036 565, https://doi.org/https://doi.org/10.1029/2022JD036565, e2022JD036565 2022JD036565, 2022.

Lenaerts, J. T. M., Van den Broeke, M. R., Déry, S. J., König-Langlo, G., Ettema, J., and Munneke, P. K.: Modelling snowdrift sublimation on an Antarctic ice shelf, The Cryosphere, 4, 179–190, https://doi.org/10.5194/tc-4-179-2010, 2010.

Li, Q., Bou-Zeid, E., Grimmond, S., Zilitinkevich, S., and Katul, G.: Revisiting the relation between momentum and scalar roughness lengths of urban surfaces, Quarterly Journal of the Royal Meteorological Society, 146, 3144–3164, https://doi.org/10.1002/qj.3839, 2020.

Loescher, H. W., Ocheltree, T., Tanner, B., Swiatek, E., Dano, B., Wong, J., Zimmerman, G., Campbell, J., Stock, C., Jacobsen, L., Shiga, Y., Kollas, J., Liburdy, J., and Law, B. E.: Comparison of temperature and wind statistics in contrasting environments among different sonic anemometer–thermometers, Agricultural and Forest Meteorology, 133, 119–139, https://doi.org/10.1016/j.agrformet.2005.08.009, 2005.

620 Mauder, M. and Foken, T.: Eddy-Covariance Software TK3, https://doi.org/10.5281/zenodo.611345, type: software, 2015.

Mauder, M. and Zeeman, M. J.: Field intercomparison of prevailing sonic anemometers, Atmospheric Measurement Techniques, 11, 249–263, https://doi.org/10.5194/amt-11-249-2018, 2018.

Mauder, M., Cuntz, M., Drüe, C., Graf, A., Rebmann, C., Schmid, H. P., Schmidt, M., and Steinbrecher, R.: A strategy for quality and uncertainty assessment of long-term eddy-covariance measurements, Agricultural and Forest Meteorology, 169, 122–135,
625 https://doi.org/10.1016/j.agrformet.2012.09.006, 2013.

Mauder, M., Foken, T., Aubinet, M., and Ibrom, A.: Eddy-Covariance Measurements, in: Springer Handbook of Atmospheric Measurements, edited by Foken, T., pp. 1473–1504, Springer International Publishing, Cham, ISBN 9783030521714, https://doi.org/10.1007/978-3-030-52171-4_55, 2021.

Miller, N. B., Turner, D. D., Bennartz, R., Shupe, M. D., Kulie, M. S., Cadeddu, M. P., and Walden, V. P.: Surface-based inversions above
630 central Greenland, Journal of Geophysical Research: Atmospheres, 118, 495–506, https://doi.org/https://doi.org/10.1029/2012JD018867, 2013.

Miller, N. B., Shupe, M. D., Cox, C. J., Noone, D., Persson, P. O. G., and Steffen, K.: Surface energy budget responses to radiative forcing at Summit, Greenland, The Cryosphere, 11, 497–516, https://doi.org/10.5194/tc-11-497-2017, 2017.

Miller, N. B., Shupe, M. D., Lenaerts, J. T. M., Kay, J. E., De Boer, G., and Bennartz, R.: Process-Based Model Evaluation Us-
635 ing Surface Energy Budget Observations in Central Greenland, Journal of Geophysical Research: Atmospheres, 123, 4777–4796, https://doi.org/https://doi.org/10.1029/2017JD027377, 2018.

Moore, C. J.: Frequency response corrections for eddy correlation systems, Boundary-Layer Meteorology, 37, 17–35, https://doi.org/10.1007/BF00122754, 1986.

Morlighem, M., Williams, C. N., Rignot, E., An, L., Arndt, J. E., Bamber, J. L., Catania, G., Chauché, N., Dowdeswell, J. A., Dorschel,
640 B., Fenty, I., Hogan, K., Howat, I., Hubbard, A., Jakobsson, M., Jordan, T. M., Kjeldsen, K. K., Millan, R., Mayer, L., Mouginot, J., Noël, B. P. Y., O'Cofaigh, C., Palmer, S., Rysgaard, S., Seroussi, H., Siegert, M. J., Slabon, P., Straneo, F., Van den Broeke, M. R., Weinrebe, W., Wood, M., and Zinglersen, K. B.: BedMachine v3: Complete Bed Topography and Ocean Bathymetry Mapping of Greenland From Multibeam Echo Sounding Combined With Mass Conservation, Geophysical Research Letters, 44, 11,051–11,061, https://doi.org/doi.org/10.1002/2017GL074954, 2017.

645 Murphy, D. M. and Koop, T.: Review of the vapour pressures of ice and supercooled water for atmospheric applications, Quarterly Journal of the Royal Meteorological Society, 131, 1539–1565, https://doi.org/https://doi.org/10.1256/qj.04.94, 2005.

Noël, B., Van de Berg, W. J., Van Wessem, J. M., Van Meijgaard, E., Van As, D., Lenaerts, J. T. M., Lhermitte, S., Kuipers Munneke, P., Smeets, C. J. P. P., Van Ulft, L. H., Van de Wal, R. S. W., and Van den Broeke, M. R.: Modelling the climate and surface mass balance of polar ice sheets using RACMO2 – Part 1: Greenland (1958–2016), The Cryosphere, 12, 811–831, https://doi.org/10.5194/tc-12-811-2018,
650 2018.

Otosaka, I. N., Shepherd, A., Ivins, E. R., Schlegel, N.-J., Amory, C., Van den Broeke, M. R., Horwath, M., Joughin, I., King, M. D., Krinner, G., Nowicki, S., Payne, A. J., Rignot, E., Scambos, T., Simon, K. M., Smith, B. E., Sørensen, L. S., Velicogna, I., Whitehouse, P. L., A, G., Agosta, C., Ahlstrøm, A. P., Blazquez, A., Colgan, W., Engdahl, M. E., Fettweis, X., Forsberg, R., Gallée, H., Gardner, A., Gilbert, L., Gourmelen, N., Groh, A., Gunter, B. C., Harig, C., Helm, V., Khan, S. A., Kittel, C., Konrad, H., Langen, P. L., Lecavalier, B. S., Liang, C.-

C., Loomis, B. D., McMillan, M., Melini, D., Mernild, S. H., Mottram, R., Mouginot, J., Nilsson, J., Noël, B., Pattle, M. E., Peltier, W. R., Pie, N., Roca, M., Sasgen, I., Save, H. V., Seo, K.-W., Scheuchl, B., Schrama, E. J. O., Schröder, L., Simonsen, S. B., Slater, T., Spada, G., Sutterley, T. C., Vishwakarma, B. D., Van Wessem, J. M., Wiese, D., Van der Wal, W., and Wouters, B.: Mass balance of the Greenland and Antarctic ice sheets from 1992 to 2020, Earth System Science Data, 15, 1597–1616, https://doi.org/10.5194/essd-15-1597-2023, 2023.

Palm, S. P., Kayetha, V., and Yang, Y.: Toward a Satellite-Derived Climatology of Blowing Snow Over Antarctica, Journal of Geophysical Research: Atmospheres, 123, 10,301–10,313, https://doi.org/https://doi.org/10.1029/2018JD028632, 2018.

Paulson, C. A.: The Mathematical Representation of Wind Speed and Temperature Profiles in the Unstable Atmospheric Surface Layer, Journal of Applied Meteorology and Climatology, 9, 857 – 861, https://doi.org/10.1175/1520-0450(1970)009<0857:TMROWS>2.0.CO;2, 1970.

Pfister, L., Lapo, K., Sayde, C., Selker, J., Mahrt, L., and Thomas, C. K.: Classifying the nocturnal atmospheric boundary layer into temperature and flow regimes, Quarterly Journal of the Royal Meteorological Society, 145, 1515–1534, https://doi.org/10.1002/qj.3508, 2019.

Plach, A., Nisancioglu, K. H., Langebroek, P. M., Born, A., and Le clec'h, S.: Eemian Greenland ice sheet simulated with a higher-order model shows strong sensitivity to surface mass balance forcing, The Cryosphere, 13, 2133–2148, https://doi.org/10.5194/tc-13-2133-2019, 2019.

Polonik, P., Chan, W., Billesbach, D., Burba, G., Li, J., Nottrott, A., Bogoev, I., Conrad, B., and Biraud, S.: Comparison of gas analyzers for eddy covariance: Effects of analyzer type and spectral corrections on fluxes, Agricultural and Forest Meteorology, 272-273, 128–142, https://doi.org/https://doi.org/10.1016/j.agrformet.2019.02.010, 2019.

Schlögl, S., Lehning, M., Nishimura, K., Huwald, H., Cullen, N. J., and Mott, R.: How do Stability Corrections Perform in the Stable Boundary Layer Over Snow?, Boundary-Layer Meteorology, 165, 161–180, https://doi.org/10.1007/s10546-017-0262-1, 2017.

Schmidt, A., Hanson, C., Chan, W. S., and Law, B. E.: Empirical assessment of uncertainties of meteorological parameters and turbulent fluxes in the AmeriFlux network, Journal of Geophysical Research: Biogeosciences, 117, https://doi.org/10.1029/2012JG002100, 2012.

Shahi, S., Abermann, J., Heinrich, G., Prinz, R., and Schöner, W.: Regional Variability and Trends of Temperature Inversions in Greenland, Journal of Climate, 33, 9391 – 9407, https://doi.org/10.1175/JCLI-D-19-0962.1, 2020.

Sigmund, A., Dujardin, J., Comola, F., Sharma, V., Huwald, H., Melo, D. B., Hirasawa, N., Nishimura, K., and Lehning, M.: Evidence of Strong Flux Underestimation by Bulk Parametrizations During Drifting and Blowing Snow, Boundary-Layer Meteorology, 182, 119–146, https://doi.org/10.1007/s10546-021-00653-x, 2022.

Smeets, C. J. P. P. and Van den Broeke, M. R.: The Parameterisation of Scalar Transfer over Rough Ice, Boundary-Layer Meteorology, 128, 339–355, https://doi.org/10.1007/s10546-008-9292-z, 2008a.

Smeets, C. J. P. P. and Van den Broeke, M. R.: Temporal and Spatial Variations of the Aerodynamic Roughness Length in the Ablation Zone of the Greenland Ice Sheet, Boundary-Layer Meteorology, 128, 315–338, https://doi.org/10.1007/s10546-008-9291-0, 2008b.

Steen-Larsen, H. C. and Wahl, S.: 2m, raw 20Hz data of wind, sonic temperature and humidity at EastGRIP site on Greenland Ice Sheet, summer 2019, https://doi.org/10.1594/PANGAEA.931439, 2021.

Steen-Larsen, H. C., Wahl, S., Box, J. E., and Hubbard, A. L.: Processed sensible and latent heat flux for summer 2016 at the EastGRIP site on the Greenland Ice Sheet - 30 min average, https://doi.pangaea.de/10.1594/PANGAEA.962310, type: dataset, a.

Steen-Larsen, H. C., Wahl, S., Box, J. E., and Hubbard, A. L.: Processed sensible and latent heat flux for summer 2017 at the EastGRIP site on the Greenland Ice Sheet - 30 min average, https://doi.pangaea.de/10.1594/PANGAEA.962311, type: dataset, b.

Steen-Larsen, H. C., Wahl, S., Box, J. E., and Hubbard, A. L.: Processed sensible and latent heat flux, friction velocity and stability at EastGRIP site on Greenland Ice Sheet, https://doi.org/10.1594/PANGAEA.946741, type: dataset, 2022.

Steen-Larsen, H. C., Haven, I., Wahl, S., Box, J. E., Hubbard, A. L., and Reuder, J.: Processed sensible and latent heat flux from a eddy-covariance systems (IRGASON) for summer 2019 at the EastGRIP, PANGAEA, https://doi.org/https://doi.org/10.1594/PANGAEA.983054, dataset, 2025a.

Steen-Larsen, H. C., Haven, I., Wahl, S., Box, J. E., Hubbard, A. L., and Reuder, J.: Processed sensible and latent heat flux from a Krypton Hygrometer (KH20) for summer 2019 at the EastGRIP, PANGAEA, https://doi.org/https://doi.org/10.1594/PANGAEA.983056, dataset, 2025b.

Steen-Larsen, H. C., Haven, I., Wahl, S., Box, J. E., Hubbard, A. L., and Reuder, J.: Processed sensible and latent heat flux from a gas analyzer (Li-COR) for summer 2019 at the EastGRIP, PANGAEA, https://doi.org/https://doi.org/10.1594/PANGAEA.983057, dataset, 2025c.

Steen-Larsen, H. C., Wahl, S., Haven, I., Box, J. E., and Hubbard, A. L.: 2m, raw 20Hz data of wind, sonic temperature and humidity from a CSAT3+KH20 at EastGRIP site on Greenland Ice Sheet, summer 2019, PANGAEA, https://doi.org/https://doi.org/10.1594/PANGAEA.982997, dataset, 2025d.

Steen-Larsen, H. C., Wahl, S., Haven, I., and Reuder, J.: 2m, raw 20Hz data of wind, sonic temperature and humidity from a CSAT3+Li-7500 at EastGRIP site on Greenland Ice Sheet, summer 2019, PANGAEA, https://doi.org/https://doi.org/10.1594/PANGAEA.982996, dataset, 2025e.

Steffen, K., Vandecrux, B., Houtz, D., Abdalati, W., Bayou, N., Box, J., Colgan, W., Espona Pernas, L., Griessinger, N., Haas-Artho, D., Heilig, A., Hubert, A., Iosifescu Enescu, I., Johnson-Amin, N., Karlsson, N., Kurup Buchholz, R., McGrath, D., Cullen, N., Naderpour, R., Molotch, N., Pedersen, A., Perren, B., Philipps, T., Plattner, G.-K., Proksch, M., Revheim, M., Særrelse, M., Schneebli, M., Sampson, K., Starkweather, S., Steffen, S., Stroeve, J., Watler, B., Winton, Ø., Zwally, J., and Ahlstrøm, A.: GC-Net Level 1 historical automated weather station data, https://doi.org/10.22008/FK2/VVXGUT, type: dataset, 2022.

Sun, J., Massman, W., and Grantz, D. A.: Aerodynamic Variables in the Bulk Formulation of Turbulent Fluxes, Boundary-Layer Meteorology, 91, 109–125, https://doi.org/10.1023/A:1001838832436, 1999.

Swinbank, W. C.: The measurement of vertical transfer of heat and water vapor by eddies in the lower atmosphere, Journal of Atmospheric Sciences, 8, 135 – 145, https://doi.org/10.1175/1520-0469(1951)008<0135:TMOVTO>2.0.CO;2, 1951.

Tanner, B., Swiatek, E., and Greene, J.: Density fluctuations and use of the krypton hygrometer in surface flux measurement, in: Management of Irrigation and Drainage Systems: Integrated Perspectives, ASCE, Park City, Utah, sponsored by the Irrigation and Drainage Division, 1993.

Town, M. S. and Walden, V. P.: Surface energy budget over the South Pole and turbulent heat fluxes as a function of an empirical bulk Richardson number, Journal of Geophysical Research: Atmospheres, 114, https://doi.org/https://doi.org/10.1029/2009JD011888, 2009.

Van As, D.: Warming, glacier melt and surface energy budget from weather station observations in the Melville Bay region of northwest Greenland, Journal of Glaciology, 57, 208–220, https://doi.org/10.3189/002214311796405898, 2011.

Van Dalum, C. T., Van de Berg, W. J., Gadde, S. N., Van Tiggelen, M., Van der Drift, T., Van Meijgaard, E., Van Ulft, L. H., and Van den Broeke, M. R.: First results of the polar regional climate model RACMO2.4, EGUsphere, 2024, 1–36, https://doi.org/10.5194/egusphere-2024-895, 2024.

Van den Broeke, M., Van As, D., Reijmer, C., and Van de Wal, R.: Assessing and Improving the Quality of Unattended Radiation Observations in Antarctica, Journal of Atmospheric and Oceanic Technology, 21, 1417 – 1431, https://doi.org/10.1175/1520-0426(2004)021<1417:AAITQO>2.0.CO;2, 2004.

Van den Broeke, M., Reijmer, C., Van As, D., Van de Wal, R., and Oerlemans, J.: Seasonal cycles of Antarctic surface energy balance from automatic weather stations, Annals of Glaciology, 41, 131–139, https://doi.org/10.3189/172756405781813168, 2005a.

Van den Broeke, M., Van As, D., Reijmer, C., and Van de Wal, R.: Sensible heat exchange at the Antarctic snow surface: a study with automatic weather stations, International Journal of Climatology, 25, 1081–1101, https://doi.org/doi.org/10.1002/joc.1152, 2005b.

Van den Broeke, M., König-Langlo, G., Picard, G., Kuipers Munneke, P., and Lenaerts, J.: Surface energy balance, melt and sublimation at Neumayer Station, East Antarctica, Antarctic Science, 22, 87, https://doi.org/10.1017/s0954102009990538, 2009.

735 Van Tiggelen, M., Smeets, P. C. J. P., Reijmer, C. H., Wouters, B., Steiner, J. F., Nieuwstraten, E. J., Immerzeel, W. W., and Van den Broeke, M. R.: Mapping the aerodynamic roughness of the Greenland Ice Sheet surface using ICESat-2: evaluation over the K-transect, The Cryosphere, 15, 2601–2621, https://doi.org/10.5194/tc-15-2601-2021, 2021.

Van Tiggelen, M., Smeets, P. C. J. P., Reijmer, C. H., Van den Broeke, M. R., Van As, D., Box, J. E., and Fausto, R. S.: Observed and Parameterized Roughness Lengths for Momentum and Heat Over Rough Ice Surfaces, Journal of Geophysical Research: Atmospheres,
740 128, e2022JD036 970, https://doi.org/https://doi.org/10.1029/2022JD036970, e2022JD036970 2022JD036970, 2023.

Van Tiggelen, M., Smeets, P. C. J. P., Reijmer, C. H., Van As, D., Box, J. E., Fausto, R. S., Khan, S. A., Rignot, E., and Van den Broeke, M. R.: Surface energy balance closure over melting snow and ice from in situ measurements on the Greenland ice sheet, Journal of Glaciology, p. 1–11, https://doi.org/10.1017/jog.2024.68, 2024.

Vandecrux, B., Box, J. E., Ahlstrøm, A. P., Andersen, S. B., Bayou, N., Colgan, W. T., Cullen, N. J., Fausto, R. S., Haas-Artho, D., Heilig, A.,
745 Houtz, D. A., How, P., Iosifescu Enescu, I., Karlsson, N. B., Kurup Buchholz, R., Mankoff, K. D., McGrath, D., Molotch, N. P., Perren, B., Revheim, M. K., Rutishauser, A., Sampson, K., Schneebeli, M., Starkweather, S., Steffen, S., Weber, J., Wright, P. J., Zwally, H. J., and Steffen, K.: The historical Greenland Climate Network (GC-Net) curated and augmented level-1 dataset, Earth System Science Data, 15, 5467–5489, https://doi.org/10.5194/essd-15-5467-2023, 2023.

Wahl, S., Steen-Larsen, H. C., Hughes, A. G., Dietrich, L. J., Zuhr, A., Behrens, M., Faber, A.-K., and Hörhold, M.:
750 Atmosphere-Snow Exchange Explains Surface Snow Isotope Variability, Geophysical Research Letters, 49, e2022GL099 529, https://doi.org/10.1029/2022GL099529, 2022.

Wang, W., Xu, J., Gao, Y., Bogoev, I., Cui, J., Deng, L., Hu, C., Liu, C., Liu, S., Shen, J., Sun, X., Xiao, W., Yuan, G., and Lee, X.: Performance Evaluation of an Integrated Open-Path Eddy Covariance System in a Cold Desert Environment, Journal of Atmospheric and Oceanic Technology, 33, 2385 – 2399, https://doi.org/10.1175/JTECH-D-15-0149.1, 2016.

755 Webb, E. K., Pearman, G. I., and Leuning, R.: Correction of flux measurements for density effects due to heat and water vapour transfer, Quarterly Journal of the Royal Meteorological Society, 106, 85–100, https://doi.org/10.1002/qj.49710644707, 1980.

Wilczak, J. M., Oncley, S. P., and Stage, S. A.: Sonic Anemometer Tilt Correction Algorithms, Boundary-Layer Meteorology, 99, 127–150, https://doi.org/10.1023/A:1018966204465, 2001.

Zuhr, A. M., Münch, T., Steen-Larsen, H. C., Hörhold, M., and Laepple, T.: Local-scale deposition of surface snow on the Greenland ice
760 sheet, The Cryosphere, 15, 4873–4900, https://doi.org/10.5194/tc-15-4873-2021, 2021.